Time-odd mean fields in covariant density functional theory: Rotating systems

A. V. Afanasjev and H. Abusara
Department of Physics and Astronomy, Mississippi State University, Mississippi State, Mississippi 39762, USA
(Received 3 April 2010; published 30 September 2010)

Time-odd mean fields (nuclear magnetism) and their impact on physical observables in rotating nuclei are studied in the framework of covariant density functional theory (CDFT). It is shown that they have profound effect on the dynamic and kinematic moments of inertia. Particle number, configuration, and rotational frequency dependencies of their impact on the moments of inertia have been analyzed in a systematic way. Nuclear magnetism can also considerably modify the band crossing features such as crossing frequencies and the properties of the kinematic and dynamic moments of inertia in the band crossing region. The impact of time-odd mean fields on the moments of inertia in the regions away from band crossing only weakly depends on the relativistic mean-field parametrization, reflecting good localization of the properties of time-odd mean fields in CDFT. The moments of inertia of normal-deformed nuclei considerably deviate from the rigid-body value. On the contrary, superdeformed and hyperdeformed nuclei have the moments of inertia which are close to rigid-body value. The structure of the currents in rotating frame, their microscopic origin, and the relations to the moments of inertia have been systematically analyzed. The phenomenon of signature separation in odd-odd nuclei, induced by time-odd mean fields, has been analyzed in detail.

DOI: 10.1103/PhysRevC.82.034329 PACS number(s): 21.10.Re, 21.60.Jz, 27.40.+z, 27.60.+j

I. INTRODUCTION

The development of self-consistent many-body theories aiming at the description of low-energy nuclear phenomena provides the necessary theoretical tools for an exploration of the nuclear chart into known and unknown regions. Theoretical methods (both relativistic [1] and nonrelativistic [2]) formulated within the framework of density functional theory (DFT) are the most promising tools for the global investigation of the properties of atomic nuclei. The power of the DFT models is essentially unchallenged in medium and heavy mass nuclei where "ab initio"–type few-body calculations are computationally impossible and the applicability of the spherical shell model is restricted to a few regions in the vicinity of doubly shell closures.

The *mean field* is a basic concept of every DFT. One can specify *time-even* and *time-odd* mean fields [3,4] dependent on the response of these fields to the action of time-reversal operator. While the properties of time-even mean fields in nuclear density functionals are reasonably well understood and defined [1,2], there are still many unknowns in our knowledge of time-odd mean fields which appear only in the nuclear systems with broken time-reversal symmetry. This is especially true in the covariant density functional theory (CDFT) [1] where only few articles were dedicated to the study of time-odd mean fields (see Ref. [5] for review). Note that the effects, produced by the magnetic potential in the Dirac equation and referred to as nuclear magnetism (NM) [6] in the framework of the CDFT, are due to time-odd mean fields.

Rotating nuclei represent a system which is strongly affected by time-odd mean fields. The representative studies of few examples [3,4,7–9] clearly show that the kinematic and dynamic moments of inertia of the nuclei rotating in collective manner are considerably affected by time-odd mean fields. It was shown in the CDFT framework [4] that the microscopic mechanism of this modification is traced back to the modifications of the expectation values of the single-particle angular momentum $\langle \hat{j}_x \rangle_i$ in the presence of NM. The contribution to $\langle \hat{j}_x \rangle_i$ due to NM is defined as

$$\Delta\langle j_x \rangle_i = \langle \hat{j}_x \rangle_i^{\mathrm{NM}} - \langle \hat{j}_x \rangle_i^{\mathrm{WNM}}, \tag{1}$$

where the subscripts NM and WNM indicate the values obtained in the calculations with and without NM, respectively. The $\Delta\langle j_x \rangle_i$ is positive at the bottom and negative at the top of the N shell [4]. The absolute value of $\Delta\langle j_x \rangle_i$ correlates with the absolute value of $\langle \hat{j}_x \rangle_i$. Note that the contributions to $\langle \hat{j}_x \rangle_i$ due to NM are small in the middle of the shell. The $\Delta\langle j_x \rangle_i$ contributions can be decomposed into the contributions due to spin ($\Delta\langle s_x \rangle_i$) and orbital ($\Delta\langle l_x \rangle_i$) angular momenta, which have complicated dependencies both on the frequency and the structure of the single-particle orbital under study [4]. Similar features are expected also in nonrelativistic DFT [4].

The changes in the alignment properties of the single-particle orbitals induced by NM [Eq. (1)] reflect themselves also in physical observables such as effective alignments and the energy splittings between signature partner orbitals (signature splitting), measured experimentally [4]. Moments of inertia and effective alignments in normal- and superdeformed nuclei in different parts of nuclear chart [1,8–14] are well described by the parametrizations which include nonlinear self-couplings only for the σ meson (see Table I in Ref. [5]). This fact strongly suggests that NM is well accounted in this type of the relativistic mean-field (RMF) parametrizations. In addition, NM can have an impact on the energy gap between the yrast and excited configurations in local minima (as illustrated on the example of the hyperdeformed minima in Ref. [15]), on the terminating states [14], and on the additivity of angular-momentum alignments [16].

A systematic investigation of time-odd mean fields in one-(two-) particle states in odd (odd-odd) nonrotating nuclei has been performed in our previous article [5]. The current

article is a continuation of our efforts aimed on comprehensive understanding of time-odd mean fields in CDFT. Its goal is a systematic study of time-odd mean fields and their manifestation in rotating nuclei.

Table I in Ref. [5] shows large variety of the parametrizations of the RMF Lagrangian. The investigation of all these parametrizations is definitely beyond the scope of this study. Thus, the present investigation has been focused on the study of time-odd mean fields in the CDFT with the parametrizations of the RMF Lagrangian including only nonlinear self-couplings of the σ meson (the group A of the parametrizations in Table I of Ref. [5]). So far, only this group of parametrizations has been used in the study of rotating nuclei [1,9–14,17,18]. The results of the study of time-odd mean fields in the groups B, C, and D of the parametrizations of meson-coupling models (Table I in Ref. [18]) as well as within the point-coupling models will be presented in a forthcoming manuscript.

The article is organized as follows. The cranked RMF theory and its details related to time-odd mean fields in rotating nuclei are discussed in Sec. II. Section III is devoted to the analysis of the impact of time-odd mean fields on band crossing features. Particle number and deformation dependencies of the impact of NM on the moments of inertia are considered in Sec. IV. Currents (and their single-particle origin) in the intrinsic frame of rotating nuclei are discussed in Sec. V. Frequency and configuration dependencies of the impact of NM on the moments of inertia are analyzed in Sec. VI. Parametrization dependence of the NM contributions to the moments of inertia are discussed in Sec. VII. Section VIII is devoted to the study of time-odd mean fields in terminating states. The phenomenon of signature separation in odd-odd nuclei is investigated in Sec. IX. Finally, Sec. X reports the main conclusions of our work.

II. THEORETICAL FORMALISM

The results presented in the current article have been obtained mainly in the framework of cranked relativistic mean-field (CRMF) theory [6,8,9]. The results obtained within the cranked relativistic Hartree-Bogoliubov (CRHB) theory [13] are shown in only a few cases. The CRMF theory has been successfully employed for the description of rotating nuclei (see Refs. [1,18] and references therein) in which time-odd mean fields play an important role. In this theory the pairing correlations are neglected which allows us to better isolate the effects induced by time-odd mean fields. The most important features of the CRMF formalism related to time-odd mean fields are outlined below (for more details see Refs. [6,9]), while the details of the CRHB theory are presented in Ref. [13].

In the Hartree approximation, the stationary Dirac equation for the nucleons in the rotating frame (in one-dimensional cranking approximation) is given by

$$(\hat{h}_D - \Omega_x \hat{J}_x)\psi_i = \varepsilon_i \psi_i, \tag{2}$$

where $\hat{h}_D$ is the Dirac Hamiltonian for the nucleon with mass m

$$\hat{h}_D = \boldsymbol{\alpha}[-i\nabla - \boldsymbol{V}(\boldsymbol{r})] + V_0(\boldsymbol{r}) + \beta[m + S(\boldsymbol{r})] \tag{3}$$

and the term

$$-\Omega_x \hat{J}_x = -\Omega_x\left(\hat{L}_x + \tfrac{1}{2}\hat{\Sigma}_x\right) \tag{4}$$

is just the Coriolis term. Note that the rotational frequency Ω_x along the x axis is defined from the condition that the expectation value of the total angular momentum at spin I has a definite value [19]

$$J(\Omega_x) = \langle \Phi_\Omega | \hat{J}_x | \Phi_\Omega \rangle = \sqrt{I(I+1)}. \tag{5}$$

The Dirac Hamiltonian contains the average fields determined by the mesons, i.e., the attractive scalar field $S(\boldsymbol{r})$

$$S(\boldsymbol{r}) = g_\sigma \sigma(\boldsymbol{r}) \tag{6}$$

and the repulsive time-like component of the vector field $V_0(\boldsymbol{r})$

$$V_0(\boldsymbol{r}) = g_\omega \omega_0(\boldsymbol{r}) + g_\rho \tau_3 \rho_0(\boldsymbol{r}) + e\frac{1-\tau_3}{2} A_0(\boldsymbol{r}). \tag{7}$$

A magnetic potential $\boldsymbol{V}(\boldsymbol{r})$

$$\boldsymbol{V}(\boldsymbol{r}) = g_\omega \boldsymbol{\omega}(\boldsymbol{r}) + g_\rho \tau_3 \boldsymbol{\rho}(\boldsymbol{r}) + e\frac{1-\tau_3}{2} \boldsymbol{A}(\boldsymbol{r}) \tag{8}$$

originates from the space-like components of the vector mesons. Note that in these equations, the four-vector components of the vector fields ω^μ, ρ^μ, and A^μ are separated into the time-like (ω_0, ρ_0, and A_0) and space-like [$\boldsymbol{\omega} = (\omega^x, \omega^y, \omega^z)$, $\boldsymbol{\rho} = (\rho^x, \rho^y, \rho^z)$, and $\boldsymbol{A} = (A^x, A^y, A^z)$] components. In the Dirac equation the magnetic potential has the structure of a magnetic field.

The corresponding meson fields and the electromagnetic potential are determined by the Klein-Gordon equations

$$\left\{-\Delta + m_\sigma^2\right\}\sigma(\boldsymbol{r}) = -g_\sigma\left[\rho_s^n(\boldsymbol{r}) + \rho_s^p(\boldsymbol{r})\right] - g_2\sigma^2(\boldsymbol{r}) - g_3\sigma^3(\boldsymbol{r}), \tag{9}$$

$$\left\{-\Delta + m_\omega^2\right\}\omega_0(\boldsymbol{r}) = g_\omega\left[\rho_v^n(\boldsymbol{r}) + \rho_v^p(\boldsymbol{r})\right], \tag{10}$$

$$\left\{-\Delta + m_\omega^2\right\}\boldsymbol{\omega}(\boldsymbol{r}) = g_\omega[\boldsymbol{j}^n(\boldsymbol{r}) + \boldsymbol{j}^p(\boldsymbol{r})], \tag{11}$$

$$\left\{-\Delta + m_\rho^2\right\}\rho_0(\boldsymbol{r}) = g_\rho\left[\rho_v^n(\boldsymbol{r}) - \rho_v^p(\boldsymbol{r})\right], \tag{12}$$

$$\left\{-\Delta + m_\rho^2\right\}\boldsymbol{\rho}(\boldsymbol{r}) = g_\rho[\boldsymbol{j}^n(\boldsymbol{r}) - \boldsymbol{j}^p(\boldsymbol{r})], \tag{13}$$

$$-\Delta A_0(\boldsymbol{r}) = e\rho_v^p(\boldsymbol{r}), \quad -\Delta\boldsymbol{A}(\boldsymbol{r}) = e\boldsymbol{j}^p(\boldsymbol{r}), \tag{14}$$

with source terms involving the various nucleonic densities and currents

$$\rho_s^{n,p}(\boldsymbol{r}) = \sum_{i=1}^{N,Z}[\psi_i(\boldsymbol{r})]^\dagger \hat{\beta}\psi_i(\boldsymbol{r}), \tag{15}$$

$$\rho_v^{n,p}(\boldsymbol{r}) = \sum_{i=1}^{N,Z}[\psi_i(\boldsymbol{r})]^\dagger \psi_i(\boldsymbol{r}), \tag{16}$$

$$\boldsymbol{j}^{n,p}(\boldsymbol{r}) = \sum_{i=1}^{N,Z}[\psi_i(\boldsymbol{r})]^\dagger \hat{\boldsymbol{\alpha}}\psi_i(\boldsymbol{r}), \tag{17}$$

where the labels n and p are used for neutrons and protons, respectively. In the equations above, the sums run over the occupied positive-energy shell-model states only (*no-sea*

approximation) [20,21]. Note that the spatial components of the vector potential $\boldsymbol{A}(\boldsymbol{r})$ are neglected in the calculations since the coupling constant of the electromagnetic interaction is small compared with the coupling constants of the meson fields.

Two terms in the Dirac equation, namely the Coriolis operator $\hat{J}_x$ and the magnetic potential $\boldsymbol{V}(\boldsymbol{r})$ (as well as the currents $\boldsymbol{j}^{n,p}(\boldsymbol{r})$ in the Klein-Gordon equations), break time-reversal symmetry [4]. Their presence leads to the appearance of time-odd mean fields. However, one should distinguish time-odd mean fields originating from Coriolis operator and magnetic potential. The Coriolis operator is always present in the description of rotating nuclei in the framework of the cranking model. However, the CRMF calculations, with only these time-odd fields accounted for, underestimate the experimental moments of inertia [8,9]. A similar situation also holds in nonrelativistic theories [3,22]. The inclusion of the currents $\boldsymbol{j}^{n,p}(\boldsymbol{r})$ into the Klein-Gordon equations, which leads to the space-like components of the vector ω and ρ mesons and thus to magnetic potential $\boldsymbol{V}(\boldsymbol{r})$, considerably improves the description of experimental moments of inertia. The effect coming from the space-like components of the vector mesons is commonly referred to as nuclear magnetism [6] since the magnetic potential has the structure of a magnetic field in the Dirac equation. Note that time-odd mean fields related to NM are defined through the Lorentz invariance [1] and thus they do not require additional coupling constants: The coupling constants of time-even mean fields are used also for time-odd mean fields.

The goal of the current article is to understand the impact of nuclear magnetism (NM) on the properties of rotating nuclei. We will use the terms *nuclear magnetism* and *time-odd mean fields* interchangeably throughout the article. However, one should keep in mind that the latter term is related only to the time-odd mean fields produced by the magnetic potential.

Single-particle orbitals are labeled at rotational frequency $\Omega_x = 0.0$ MeV by $[Nn_z\Lambda]\Omega^{\rm sgn}$. $[Nn_z\Lambda]\Omega$ are the asymptotic quantum numbers (Nilsson quantum numbers) of the dominant component of the wave function. The superscripts sgn to the orbital labels are used sometimes to indicate the sign of the signature r for that orbital ($r = \pm i$). Note that the labeling by means of Nilsson labels is performed only when the calculated shape of nuclear configuration is prolate or near-prolate.

Many-particle configurations (further nuclear configurations or configurations) are specified by the occupation of available single-particle orbitals. In the calculations without pairing, the occupation numbers n are integer ($n = 0$ or 1). In addition, in the CRMF code it is possible to specify the occupation of either $r = +i$ or $r = -i$ signature of the single-particle state. In odd-odd nuclei, all single-particle states of specific (proton and neutron) subsystem with exception of one are pairwise occupied. We will call this occupied single-particle state of fixed signature for which its time-reversal (signature) counterpart state is empty as *blocked state* in order to simplify the discussion. The specification of nuclear configuration by means of listing all occupied single-particle states is unpractical. Thus, in odd-odd nuclei the Nilsson labels of the blocked proton and neutron states and their signatures are used for configuration labeling.

The CRMF equations are solved in the basis of an anisotropic three-dimensional harmonic oscillator in Cartesian coordinates characterized by the deformation parameters β_0 and γ as well as the oscillator frequency $\hbar\omega_0 = 41A^{-1/3}$ MeV. Our selection of the deformation parameters of the basis is the same as in earlier systematic studies of rotating nuclei in different regions of nuclear chart (Refs. [9–11,13,18]). $\gamma = 0^\circ$ is used in all calculations. The deformation parameter β_0 of the basis is selected in such a way that it provides the convergence to the local minimum under study. Thus, $\beta_0 = 0.25$ is used in the case of normal-deformed (ND) states, $\beta_0 = 0.2$ and $\beta_0 = 0.5$ in the case of superdeformed (SD) states in the $A \sim 60$ and $A \sim 150$, 190 mass regions, respectively, and $\beta_0 = 1.0$ in the case of the hyperdeformed (HD) states. The truncation of basis is performed in such a way that all states belonging to the shells up to fermionic $N_F = 12$ and bosonic $N_B = 20$ are taken into account in the calculations of ND and SD states. The fermionic basis is increased up to $N_F = 14$ in the calculations of HD states. Numerical analysis indicates that these truncation schemes provide sufficient numerical accuracy for the physical quantities of interest (see Refs. [9–11,13,18]). The majority of the calculations are performed with the NL1 parametrization [21] of the RMF Lagrangian since this parametrization has been used extensively in earlier systematic studies of rotating nuclei across the nuclear chart [9–11,13,14,18].

To investigate the impact of NM (time-odd mean fields) on physical observables, the CRMF calculations are performed in two calculational schemes for fixed configurations:

(i) Fully self-consistent calculations with NM included (hereafter denoted NM calculations), which take into account space-like components of the vector mesons [Eqs. (11), (13), and (8)], currents [Eqs. (11), (13), and (17)], and magnetic potential $\boldsymbol{V}(\boldsymbol{r})$ [(Eq. (8)].

(ii) Fully self-consistent calculations without NM (hereafter denoted as WNM calculations), which omit space-like components of the vector mesons [Eqs. (11), (13), and (8)], currents in the Klein-Gordon equations [Eqs. (11) and (13), and magnetic potential $\boldsymbol{V}(\boldsymbol{r})$ (Eq. (8)]. The results of the NM and WNM calculations are always compared for the same nuclear configuration.

These are the ways in which the effects of time-odd mean fields can be studied, and as such they are frequently used in DFT studies of rotating systems, both in relativistic and in nonrelativistic frameworks [3,4,8,14,22]. One should, however, keep in mind that if time-odd fields are neglected, the local Lorentz invariance (Galilean invariance in nonrelativistic framework [3,23]) is violated. The inclusion of time-odd mean fields restores the Lorentz invariance.

It is interesting to compare the basic features such as Lorentz invariance and the definition of the coupling constants of the time-odd channel of the CDF theory discussed above with the ones of nonrelativistic Skyrme energy-density functional (EDF) theory. It was recognized in earlier Skyrme DFT studies that the connection between the coupling constants of time-odd and time-even channels depends on what

entity, namely Skyrme force or energy density functional is considered to be more fundamental [3,23,24]. If the Skyrme force is considered more fundamental then the time-odd constants are determined as a function of time-even constants [3,24]. However, since the time-even coupling constants are usually adjusted solely to the time-even observables, the resulting values of the time-odd coupling constants simply "fictitious" or "illusory," as noted already in Ref. [25] (see also Ref. [24]). On the contrary, in the framework of the Skyrme energy density functional theory, time-odd properties of the functional are independent of time-even properties which is a consequence of broken link between the Skyrme force and the density functional.

The question of whether Galilean invariance must be imposed in Skyrme EDF is not yet resolved [23], despite the fact that it is imposed in many studies. Note that in many phenomenological approaches, such as the noninteracting or interacting shell models, Galilean symmetry is not considered, because the translational motion is not within the scope of such models [23]. It is also important to mention that the cranking models based on phenomelogical Woods-Saxon or Nilsson potentials do not incorporate time-odd mean fields. However, they successfully describe rotating nuclei [26,27].

Note that the Coriolis term is present in NM and WNM calculations. This means that the currents [Eq. (17)] are always present in rotating nuclei. However, it is important to distinguish the currents induced by the Coriolis term and the ones which appear due to magnetic potential. The currents, which appear in the WNM calculations, are generated by the Coriolis term. Thus, we will call them *Coriolis-induced currents*. On the contrary, the currents in the NM calculations are generated by both the Coriolis term and magnetic potential. The difference of the currents in the NM and WNM calculations is attributable to magnetic potential. Thus, the currents $[\boldsymbol{j}^{n,p}(\boldsymbol{r})]^{\mathrm{NM}} - [\boldsymbol{j}^{n,p}(\boldsymbol{r})]^{\mathrm{WNM}}$ will be called *magnetic potential–induced currents*.

In the following, the contribution $\Delta O^{\mathrm{NM-contr}}$ (in percentage points) of NM to the physical observable O is defined as

$$\Delta O^{\mathrm{NM-contr}} = \frac{O^{\mathrm{NM}} - O^{\mathrm{WNM}}}{O^{\mathrm{NM}}} \times 100\%. \qquad (18)$$

The physical observables, most frequently used in the analysis of rotating nuclei, are kinematic $[J^{(1)}]$ and dynamic $[J^{(2)}]$ moments of inertia which are defined as

$$J^{(1)}(\Omega_x) = \frac{J}{\Omega_x}, \qquad J^{(2)}(\Omega_x) = \frac{dJ}{d\Omega_x}, \qquad (19)$$

where J is the expectation value of the total angular momentum along the x axis. In the CRMF theory, this quantity is defined as a sum of the expectation values of the single-particle angular-momentum operators $\hat{j}_x$ of the occupied states

$$J = \sum_i \langle i|\hat{j}_x|i\rangle. \qquad (20)$$

Thus, the modifications of the moments of inertia due to NM can be traced back to the changes of the single-particle expectation values $\langle \hat{j}_x\rangle_i = \langle i|\hat{j}_x|i\rangle$ and the corresponding contributions of spin ($\langle \hat{s}_x\rangle_i$) and orbital ($\langle \hat{l}_x\rangle_i$) angular momenta [4].

III. NUCLEAR MAGNETISM AND BAND CROSSING FEATURES

Since NM substantially modifies the single-particle properties (energies and alignments) [1,4], it is reasonable to expect that the band crossing features are affected by NM. In order to study this question, the CRMF (without pairing) and the CRHB + LN calculations have been performed for lowest superdeformed (SD) band in ^{194}Pb. In the CRHB + LN calculations, the D1S Gogny force [28] is used in pairing channel and an approximate particle number projection is performed by means of the Lipkin-Nogami method [13].

The unpaired proton band crossing seen in the CRMF calculations originates from the interaction between the $\pi[642]5/2^+$ and $\pi[651]1/2^+$ orbitals [Fig. 1(a)]. Since NM increases the single-particle alignment $\langle \hat{j}_x\rangle_i$ [Fig. 1(b)] and the slope of the Routhian for the $\pi[651]1/2^+$ orbital somewhat [Fig. 1(a)], the band crossing takes place at lower frequency. The shift of crossing frequency due to NM is considerable (120 keV) from 0.465 MeV (WNM) down to 0.345 MeV (NM) [Fig. 1(a)]. The calculations also suggest that the strength of the interaction between two interacting orbitals at the band crossing is modified in the presence of NM as seen in the change of the energy distance (gap) between these two orbitals at the crossing frequency [Fig. 1(a)].

An additional mechanism affecting the band crossing frequencies will be active in odd and odd-odd mass nuclei as well as in excited configurations of even-even nuclei. In such configurations, there is at least one single-particle state the opposite signature of which is not occupied. This results

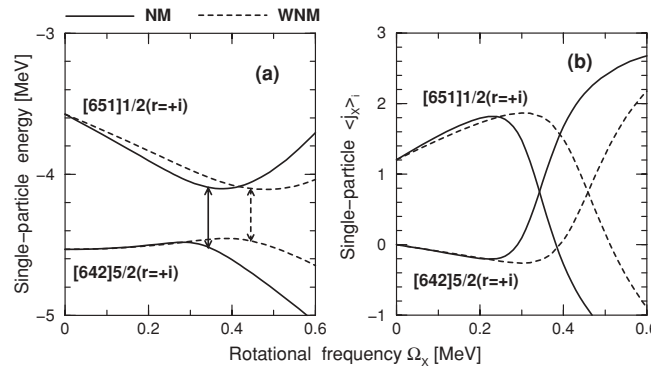

FIG. 1. (a) Proton single-particle energies (Routhians) in the self-consistent rotating potential as a function of rotational frequency Ω_x obtained in the CRMF calculations with and without NM. They are given along the deformation path of the lowest SD configuration in ^{194}Pb. Only interacting $[651]1/2^+$ and $[642]5/2^+$ orbitals are shown, see Fig. 1 in Ref. [13] for full spectra. (b) The expectation values $\langle \hat{j}_x\rangle_i$ of the single-particle angular-momentum operator $\hat{j}_x$ of the orbitals shown in (a). Solid and dashed arrows are used to indicate the frequencies [as well as the energy gap between the interacting orbitals in (a)] at which the band crossings take place in the calculations with and without NM, respectively.

in the currents at $\Omega_x = 0.0$ MeV [5]. The energy splitting between different signatures of the single-particle states at no rotation is a typical consequence of these currents (see Sec. IV A in Ref. [5] for more details). As a result, the energy gap between interacting orbitals at $\Omega_x = 0.0$ MeV can become larger or smaller dependent on the impact of the currents on the single-particle energies of interacting states. Consequently, this change in the energy gap will translate into higher or lower band crossing frequencies. Note that for simplicity we assume that the $\Omega_x = 0.0$ currents will not modify the alignment properties of interacting orbitals; this translates into the independence of the single-particle Routhian slope in the energy versus Ω_x plot [see, for example, Fig. 1(a)] on the $\Omega_x = 0.0$ currents.

Figure 1(a) can be used to illustrate this mechanism. Let assume that the $\Omega_x = 0.0$ currents will increase the energy gap between the $\pi[642]5/2^+$ and $\pi[651]1/2^+$ orbitals at $\Omega_x = 0.0$ MeV: This will lead to higher band crossing frequencies. However, the band crossing frequencies will decrease in the case when the energy gap between these orbitals at $\Omega_x = 0.0$ MeV becomes smaller in the presence of the $\Omega_x = 0.0$ currents. The assumption that the $\Omega_x = 0.0$ currents do not have an impact on the alignment properties of interacting orbitals is definitely too simplistic but it allows us to illustrate the fact that NM can both decrease and increase the band crossing frequencies. This mechanism is not active in the configuration of even-even ^{194}Pb nucleus discussed above since both signatures of all states below the Fermi level are pairwise occupied. As a result, no current is present at $\Omega_x = 0.0$ MeV.

The impact of NM on band crossing features is also seen in the CRHB + LN calculations where the alignment of the pairs of $j_{15/2}$ neutrons and $i_{13/2}$ protons causes the shoulder and peak in total dynamic moment of inertia $J^{(2)}$ [Fig. 2(c)] (see also Ref. [13]). Note that each of these two alignments creates a peak in the dynamic moment of inertia of corresponding subsystem. NM shifts the paired neutron band crossing to lower frequencies by 70 keV from 0.485 MeV (WNM) to 0.415 MeV (NM). Paired proton band crossing lies in the calculations with NM at $\Omega_x = 0.535$ MeV, while only the beginning of this crossing is seen in the calculations without NM [Fig. 2(c)].

The origin of this effect is twofold. Similar to the unpaired calculations, the part of it can be traced to the fact that NM increases the expectation values $\langle \hat{j}_x \rangle_i$ of the orbitals located at the bottom of the shell (the discussed orbitals are of this kind) [4]. The corresponding larger slope of the quasiparticle Routhians causes the shift of the crossing to lower frequencies. However, an additional contribution comes from the modification of the pairing by NM. There is a difference in the pairing energies calculated with and without NM which increases with rotational frequency, see Figs. 3(c) and 3(d). The pairing in the calculations with NM is weaker. This can be explained by the increase of $\langle \hat{j}_x \rangle_i$ of the orbitals located at the bottom of the shell due to NM (see above). The gradual breaking of high-j pairs proceeds faster, which is reflected in a faster decrease of pairing with increasing Ω_x. Thus we can specify this effect as an antipairing effect induced by NM.

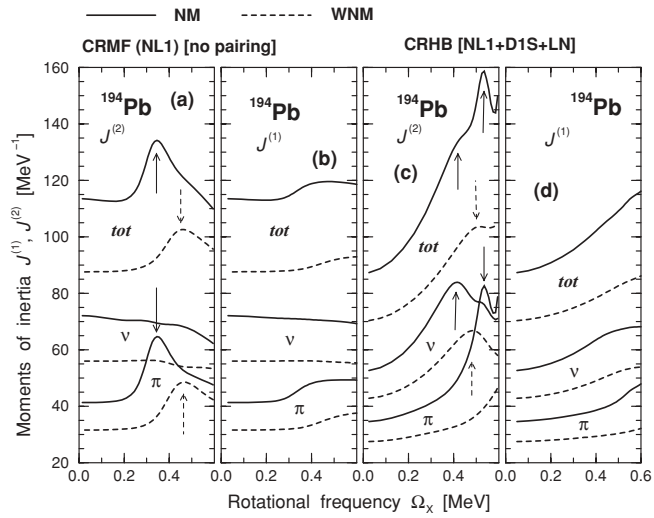

FIG. 2. Kinematic ($J^{(1)}$) and dynamic ($J^{(2)}$) moments of inertia for the lowest SD configuration in ^{194}Pb obtained in the calculations with and without NM. Proton and neutron contributions to these quantities are indicated by π and ν, while total moments are indicated by *tot*. Panels (a) and (b) show the results obtained in the calculations without pairing, while panels (c) and (d) show the results of the calculations within the CRHB + LN framework. Solid and dashed arrows are used to indicate the frequencies at which the band crossings take place in the calculations with and without NM, respectively.

These considerable differences in the crossing frequencies obtained in the calculations with and without NM cannot be attributed to the differences in equilibrium deformations, since calculated transition quadrupole moments Q_t and mass hexadecapole moments Q_{40} obtained in the calculations with and without NM differ only marginally before band crossing; see Figs. 3(a) and 3(b).

The influence of time-odd mean fields on band crossing features has been studied by means of a schematic non–self-consistent model based on the Skyrme forces in Ref. [7]. In this study, time-odd fields emerging from the $\mathbf{S}^2$ and $-\mathbf{S}\Delta\mathbf{S}$ terms of the Skyrme Hamiltonian shift the alignment of the $i_{13/2}$ neutron pair to higher frequencies in ^{158}Dy. On the contrary, this crossing appears at lower frequencies in the CRHB + LN calculations when NM is taken into account. This difference is not surprising considering the fact that time-odd mean fields are not well defined in nonrelativistic density functional theories [3,29]. It was also suggested in the cranked Skyrme Hartree-Fock framework that time-odd mean fields may be responsible for band crossing in yrast superdeformed band of ^{60}Zn [30]. However, this crossing is described as paired band crossing in the CRHB + LN calculations [31].

Above discussed CRMF and CRHB + LN examples clearly show that the modifications of band crossing features (crossing frequencies and the features of the kinematic and dynamic moments of inertia in band crossing region) caused by NM are substantial and depend on the underlying modifications of single-particle properties such as alignments and single-particle (quasiparticle) energies.

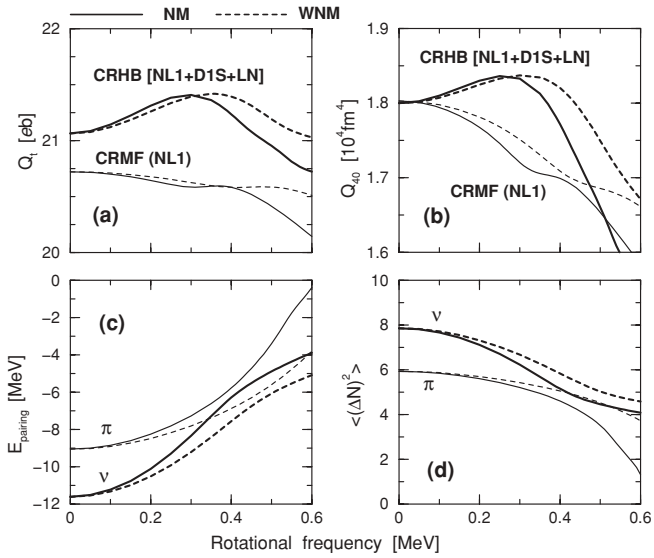

FIG. 3. Transition quadrupole moments Q_t (a), mass hexadecapole moments Q_{40} (b), proton and neutron pairing energies $E_{\text{pairing}} = -1/2\text{Tr}\,(\Delta\kappa)$ (c) and proton and neutron particle number fluctuations $\langle(\Delta\hat{N})^2\rangle$ (d) of the lowest SD solution in ^{194}Pb obtained in the calculations with and without NM. Thick and thin lines in the upper panels are used for the results obtained in the CRHB and CRMF theories, respectively. On the bottom panels, thick and thin lines are used for neutron and proton quantities, respectively.

IV. PARTICLE NUMBER AND DEFORMATION DEPENDENCIES OF THE IMPACT OF NUCLEAR MAGNETISM ON THE MOMENTS OF INERTIA

In the current section, the particle number and deformation dependencies of the impact of NM on the kinematic moments of inertia are discussed in detail. We consider the contribution of NM to kinematic moment of inertia, namely the $[J^{(1)}_{\text{NM}} - J^{(1)}_{\text{WNM}}]/J^{(1)}_{\text{NM}}$ quantity, and its variations as a function of particle number and deformation. In addition, we investigate how close fully self-consistent value of the kinematic moment of inertia comes to the rigid-body moment of inertia J_{rig}. The latter quantity is obtained in one-dimensional cranking approximation with the rotation defined around the x axis from the calculated density distribution $\rho(\boldsymbol{r})$ by

$$J_{\text{rig}} = \int \rho(\boldsymbol{r})(y^2 + z^2)\, d^3r. \tag{21}$$

The contributions of NM to kinematic moment of inertia (the $[J^{(1)}_{\text{NM}} - J^{(1)}_{\text{WNM}}]/J^{(1)}_{\text{NM}}$ quantity) for normal deformed bands in a number of isotope chains with proton number $Z \geqslant 50$ are shown as a function of neutron number in Fig. 4. Only the cases in which the nuclear configurations are the same in the calculations with and without nuclear magnetism are shown in this figure. NM typically increases the calculated kinematic moments of inertia by 10–30%. However, this increase is around 40% in the $N = 108, 110$ W isotopes. Considerable fluctuations of the $[J^{(1)}_{\text{NM}} - J^{(1)}_{\text{WNM}}]/J^{(1)}_{\text{NM}}$ quantity as a function of neutron number seen in some isotope chains are due to the changes in underlying single-particle structure. Large changes in the $[J^{(1)}_{\text{NM}} - J^{(1)}_{\text{WNM}}]/J^{(1)}_{\text{NM}}$ quantity are seen

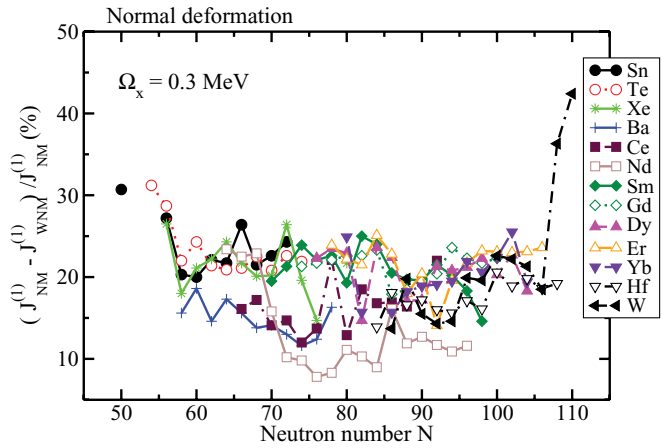

FIG. 4. (Color online) The contribution (in percentage points) of NM to the kinematic moments of inertia of nuclei in different isotope chains at normal deformation. The results for the lowest in energy solutions are shown at rotational frequency $\Omega_x = 0.3$ MeV. The frequency has been fixed at this value in order to make the comparison with the results of Ref. [32] straightforward.

on going from the isotope with neutron number N to the isotope with $N + 2$ when two neutron single-particle orbitals, by which the configurations of compared nuclei differ, have the expectation values of the single-particle angular momenta $\langle\hat{j}_x\rangle_i$ strongly affected by NM. The opposite is also true when two neutron single-particle orbitals, by which the configurations of compared nuclei differ, have the expectation values of the single-particle angular momenta $\langle\hat{j}_x\rangle_i$ that are only marginally affected by NM. Note that in some cases proton configurations of two neighboring nuclei with neutron numbers N and $N + 2$ are also different due to the deformation changes; this also contributes into the fluctuations of the $[J^{(1)}_{\text{NM}} - J^{(1)}_{\text{WNM}}]/J^{(1)}_{\text{NM}}$ quantity as a function of neutron number.

One can also extract from Fig. 4 the dependence of the contributions of NM to kinematic moments of inertia on proton number Z by considering the results of the calculations at constant value of neutron number N. Such analysis reveals the fluctuations in the $[J^{(1)}_{\text{NM}} - J^{(1)}_{\text{WNM}}]/J^{(1)}_{\text{NM}}$ quantities which are similar to the ones discussed above. The origin of these fluctuations can again be traced back to the changes (as a function of proton number) in underlying single-particle structure.

Figure 5 compares rigid-body moments of inertia J_{rig} [Eq. (21)] with fully microscopic kinematic moments of inertia $J^{(1)}_{\text{NM}}$ [Eqs. (19) and (20)] obtained in the calculations with NM using the $[J_{\text{rig}} - J^{(1)}_{\text{NM}}]/J_{\text{rig}}$ quantity. One can see that considerable deviations (in majority of the cases being in the window of $\pm 30\%$ but reaching $\pm 60\%$ in some nuclei) between these two moments of inertia are observed at normal deformation.

The analysis within the framework of the periodic orbit theory [32] concluded that the deviations of the moments of inertia from the rigid-body value at high spin are determined by the shell structure of a system of independent fermions confined by a leptodermous potential. For the case of prolate deformation and the rotation perpendicular to the symmetry

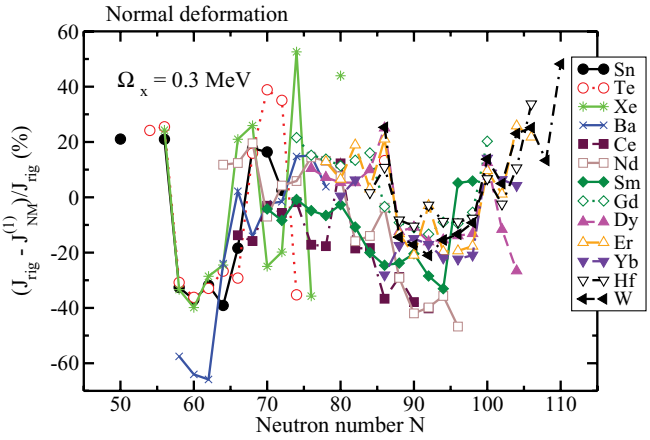

FIG. 5. (Color online) The difference (in percentage points) between the rigid-body moments of inertia $J_{\rm rig}$ and kinematic moments of inertia calculated with NM for the nuclear configurations shown in Fig. 4.

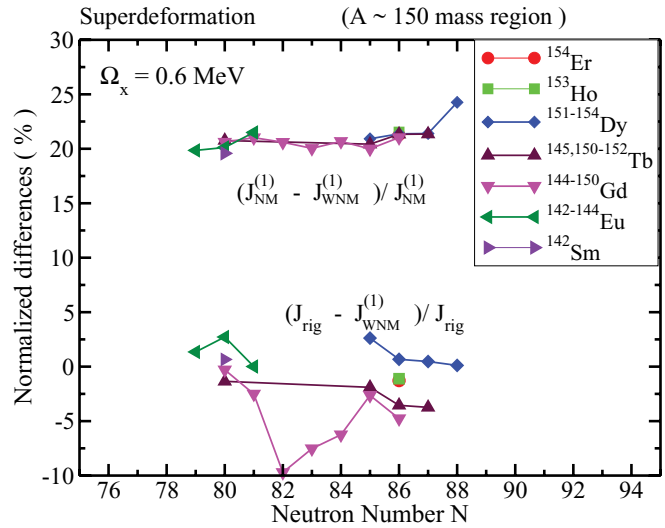

FIG. 6. (Color online) The contribution $[J^{(1)}_{\rm NM} - J^{(1)}_{\rm WNM}]/J^{(1)}_{\rm NM}$ (in percentage points) of NM to the kinematic moments of inertia and the difference $[J_{\rm rig} - J^{(1)}_{\rm NM}]/J_{\rm rig}$ (in percentage points) between the rigid-body moments of inertia and kinematic moments of inertia calculated with inclusion of NM. The results for yrast SD configurations in the $A \sim 150$ mass region of superdeformation are shown at rotational frequency $\Omega_x = 0.6$ MeV for nuclei which were previously analyzed in the CRMF calculations in Refs. [9,10].

axis (the majority of the cases studied in the current article fall under this category), the meridian orbits determine the shell moments of inertia because only they enclose rotational flux [32].

Large similarities are seen between the results of our calculations and the ones based on the cranked Woods-Saxon potential in Ref. [32]. For example, the right bottom panel in Fig. 10 of Ref. [32] shows the difference $J_{\rm pper} - J_{\rm rig}$ between the moments of inertia $J_{\rm pper}$ calculated in the cranked Woods-Saxon potential and rigid-body moments of inertia $J_{\rm rig}$ for the case of prolate deformation and the rotation around the axis perpendicular to the symmetry axis. If one corrects for the difference in the representation of calculated quantities $\{(J_{\rm pper} - J_{\rm rig})$ in Ref. [32] and $[J_{\rm rig} - J^{(1)}_{\rm NM}]/J_{\rm rig}$ in the present article$\}$, then one can see that our results show similar shell dependence of the $[J^{(1)}_{\rm NM} - J^{1}_{\rm rig}]$ quantities as the one seen in Fig. 10 of Ref. [32]. Some differences between these two calculations are in part due to simplistic method of the calculation of the rigid-body moments of inertia in Ref. [32] (see Sec. II B of Ref. [32] for details).

The CRMF calculations describe rather well the kinematic moments of inertia of normal-deformed [12,33] and smooth-terminating [1,33] bands at high spin where the pairing is negligible. Experimental data on kinematic moments of inertia of normal-deformed rotational bands at low spin [which are strongly affected by pairing] are also well described in the cranked relativistic Hartree-Bogoliubov calculations [17,34]. These results together with the ones presented in the current article strongly support the conclusion that weakly and normal-deformed nuclei show the moments of inertia which strongly deviate from the rigid-body value (see also Refs. [26,32]).

Figures 6 and 7 show the results of calculations for yrast SD configurations in the $A \sim 150$ mass region of superdeformation and for yrast hyperdeformed (HD) configurations in the $Z = 40$–58 part of the nuclear chart, respectively. It is clearly seen that the $[J^{(1)}_{\rm NM} - J^{(1)}_{\rm WNM}]/J^{(1)}_{\rm NM}$ and $[J_{\rm rig} - J^{(1)}_{\rm NM}]/J_{\rm rig}$ quantities at these extreme deformations show much smaller fluctuations than the ones at normal deformation. Indeed, the contribution of NM into kinematic moment of inertia at SD and HD is in a narrow 20–27% range (Figs. 6 and 7), while it covers a much larger 9–43% range at normal deformation (Fig. 4). In addition, the values of kinematic moment of inertia calculated with NM are typically within 5% of the rigid-body value for the moment of inertia at SD and HD (Figs. 6 and 7), while much larger fluctuations (typically within 40% of the

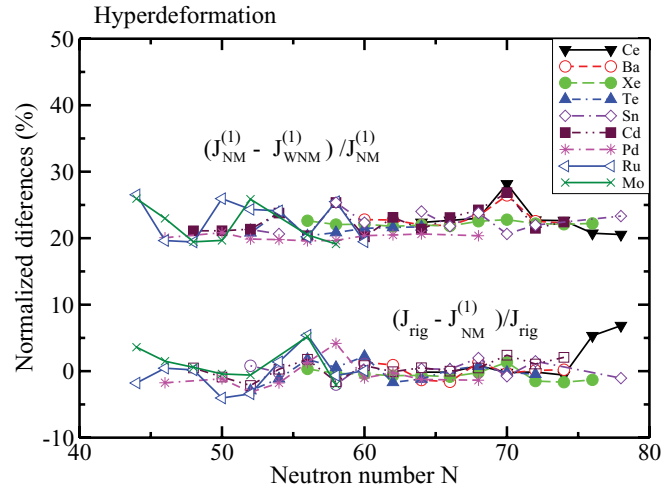

FIG. 7. (Color online) The same as in Fig. 6 but for the hyperdeformed configurations. The results of the calculations are shown for the yrast HD configurations, studied in the systematic survey of the hyperdeformation in the $Z = 40$–58 region of the nuclear chart [15,18], at spins at which they become yrast (rotational frequency $\Omega_x \approx 0.8$–1.0 MeV).

rigid-body value) are seen in the case of normal deformation (Fig. 5).

Microscopic origin of these features can be traced back to the underlying shell structure. The analysis within the periodic orbit theory [32] shows that the single-particle orbits that cause shell structure of prolate superdeformed nuclei do not carry rotational flux if the axis of rotation is perpendicular to the symmetry axis. Therefore, the moments of inertia of the SD bands in such nuclei should be equal to the rigid-body value [32]. Such conclusion is in general supported by our microscopic calculations which show that the calculated moments of inertia are typically within 5% of the rigid-body value. The experimental deviations (obtained under spin assignments of Refs. [10,35]) from the rigid-body values are about 6% or less in the $A \sim 150$ region of superdeformation (see Fig. 5 in Ref. [32]). We also expect that similar mechanism is also responsible for the observed features of the moments of inertia at HD. However, the periodic orbit theory analysis of such features is not available and it goes beyond the scope of the current article.

V. CURRENTS IN INTRINSIC (ROTATING) FRAME OF COLLECTIVELY ROTATING NUCLEI

Current distributions in the intrinsic (rotating) frame have been studied earlier in several publications. It is well known that there are no currents in the intrinsic frame if the rigid nonspherical body rotates uniformly (rigid rotation) (see Sec. IV A-V in Ref. [36]). The general aspects of the velocity (current) fields have been discussed in detail in the framework of single-particle Schrödinger fluid [37], which exhibits a remarkably rich variety of fluid dynamical features, including compressible flow and line vortices. Nuclear intrinsic vorticity and its coupling to global rotations have been studied within the so-called Routhian approach both in the semiclassical approach [38,39] and in fully self-consistent cranked Hartree-Fock and Hartree-Fock-Bogoliubov approaches based on the Skyrme force [40]. The current distributions in rotating frame have been studied in phenomenological cranking approaches based on harmonic oscillator [38,41–43] and Nilsson [44] potentials and in self-consistent cranking approaches based on the Skyrme force [40,45]. Note that the intrinsic current field (as any vector field according to the Hemholtz's theorem) can be split into irrotational and intrinsic vortical fields [39].

Figure 8 shows typical current distributions obtained in the CRMF calculations for selected normal-, super-, and hyperdeformed nuclei. Despite the fact that the moments of inertia of the SD and HD configurations are very close to the rigid-body values (Sec. IV), the presence of strong vortices[1] demonstrates the dramatic deviation of the currents from rigid rotation. For example, the HD configurations in ^{92}Mo [Fig. 8(a)] and ^{108}Cd [Fig. 8(b)] show two strong vortices centered at $z \approx \pm 2$ fm. Note that the vortices (i.e., the curl) of the current fields are aligned or antialigned along a principal x axis of the ellipsoid because of the use of one-dimensional cranking approximation. On the other hand, the HD configuration in ^{118}Te [Fig. 8(c)] shows one very strong vortice centered at $z = 0$ fm, and 2 weaker vortices centered at $z \approx \pm 4.5$ fm. All three vortices rotate clockwise. The currents in the rotating frame of reference that is fixed to the body are caused by quantized motion of the fermions. Thus, the differences between the currents in ^{92}Mo and ^{108}Cd on one hand and the ones in ^{118}Te on the other hand are caused by the differences in the underlying single-particle configurations. Contrary to the HD configurations, the current distributions in the SD configurations of ^{142}Sm, ^{148}Gd, and ^{152}Dy are characterized by a single very strong central vortice [Figs. 8(d)–8(f). Current patterns in normal deformed nuclei ^{100}Sn and ^{118}Ba look more disordered than in the SD and HD nuclei [Figs. 8(g) and 8(h)]. This is because three (four) large vortices in ^{100}Sn (^{118}Ba) are spread out over the volume of the nucleus. On the other hand, the current pattern is dominated by a single large central vortice in the ND configuration of ^{136}Nd [Fig. 8(i)].

Note that all considered configurations are characterized by the weak current in the surface area. On the contrary, the average intrinsic current flows mainly in the nuclear surface in the semiclassical description of currents in normal and superfluid rotating nuclei [38]. This underlines the importance of quantum mechanical treatment of the currents.

The total current is the sum of Coriolis-induced and magnetic potential–induced currents. Total current is dominated by the Coriolis-induced currents; magnetic potential–induced currents represent approximately 5–20% (30%) of total current in the HD and SD [ND] nuclei shown in Fig. 8. The only exception is ^{92}Mo, in the central region, of which magnetic potential–induced currents are larger than Coriolis-induced currents by a factor close to 2. The spatial distribution of Coriolis-induced and magnetic potential–induced currents is similar in the majority of nuclei shown in Fig. 8. However, the spatial distribution of these two types of currents differ substantially in ^{92}Mo, ^{146}Gd, and ^{118}Ba.

Comparing current patterns shown in Fig. 8, one can conclude that for a system of noninteracting fermions, the total current, being the sum of the single-particle currents [see Eq. (17)], is, in general, quite complicated. This is a consequence of the fact that the localization, the strength, and the structure of the current vortices created by a particle in a specific single-particle state depend on its nodal structure (see Ref. [43] and Sec. III C in Ref. [5]). In this respect it is important to mention the results of Ref. [43] which showed that Coriolis-induced current for a single-particle in a slowly rotating anisotropic harmonic oscillator potential has, in fact, a rather simple structure. It exhibits a number of localized circulations with precisely predictable centers and sense of rotation. The centers of the circulations are found at the nodes and peaks of the oscillator eigenfunctions, thus, forming a rectangular array somewhat similar to a crystal lattice.

The wave function of the CRMF approach is more complicated than that of a rotating anisotropic harmonic oscillator because of the presence of spin-orbit interaction and the split of the wave function into large and small components.

[1]The existence of vortices at these points implies nonvanishing current circulations which are defined as $\boldsymbol{C}(\boldsymbol{r}) = \boldsymbol{\nabla} \times \boldsymbol{j}(\boldsymbol{r})$ [43].

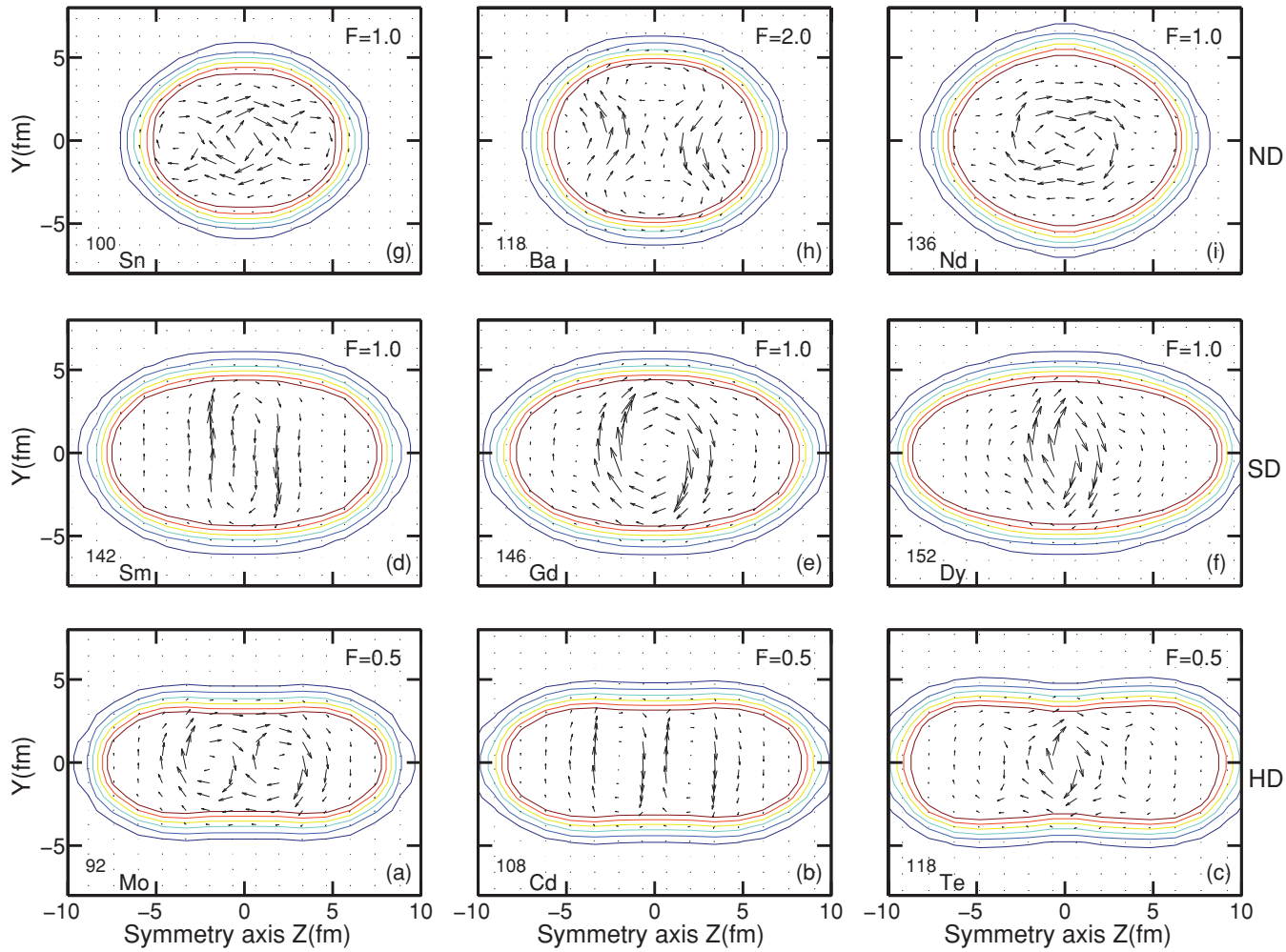

FIG. 8. (Color online) Total neutron current distributions $\boldsymbol{j}^n(\boldsymbol{r})$ in the intrinsic frame in the y-z plane for several normal-deformed (ND) (upper row), superdeformed (SD) (middle row), and hyperdeformed (HD) (bottom row) configurations in different nuclei. They are shown at $x \approx 0.48$ fm in the case of ND and SD configurations and at $x \approx 0.42$ fm in the case of HD configurations. The results of calculations are shown at rotational frequencies $\Omega_x = 0.3$ MeV and $\Omega_x = 0.5$ MeV for the ND and SD configurations, respectively, and at the spin ($\Omega_x \sim 1.0$ MeV) at which the HD configurations become yrast (see Ref. [18] for details) in the case of HD configurations. The currents in panels (d)–(g) and (i) are plotted at arbitrary units for better visualization. The currents in other panels are normalized to the currents in panels (d)–(g) and (i) by using factor F. This factor is chosen in such way that the current distribution for every nucleus is clearly seen. The shape and size of the nucleus are indicated by density lines which are plotted in the range 0.01–0.06 fm^{-3} in step of 0.01 fm^{-3}.

Moreover, there are magnetic potential–induced currents in addition to Coriolis-induced ones. However, the analysis of single-particle vortices in rotating nuclei in general confirms the observations made in Ref. [43]. The typical features of the single-particle currents in the CRMF approach are considered below on the example of three neutron single-particle states occupied in the yrast SD configuration of ^{152}Dy. The current and density distributions of these states are shown in Fig. 9. Let us first consider the $\nu[642]5/2^+$ state. The comparison of Figs. 9(c) and 9(d) reveals that the rotation of a nucleus considerably increases the currents in this state. On the other hand, the density distribution is almost unaffected by rotation. The rotation of a nucleus also leads to a change in the structure of the circulations. At $\Omega_x = 0.0$ MeV, there are three weak circulations centered around the nodes at ($y = 0$ fm, $z = 0$ fm) and ($y = 0$ fm, $z \approx \pm 4$ fm); they are due to magnetic potential. Only two much stronger circulations are visible at $\Omega_x = 0.5$ MeV: they are centered around the nodes located at ($y = 0$ fm, $z \approx \pm 2.5$ fm). This change of the structure of vortices can be attributed to additional currents produced by the Coriolis term as well as to the change of the structure of wave function with increasing rotational frequency. The wave function in terms of two largest components has the 86%[642]5/2+5%[633]5/2 and 63%[642]5/2+13%[651]3/2 structure[2] at $\Omega_x = 0.0$ MeV and $\Omega_x = 0.5$ MeV, respectively.

[2]The percentage points show the weights of respective components of the wave function in the total structure of the wave function. Note that only two largest components of the wave function are displayed.

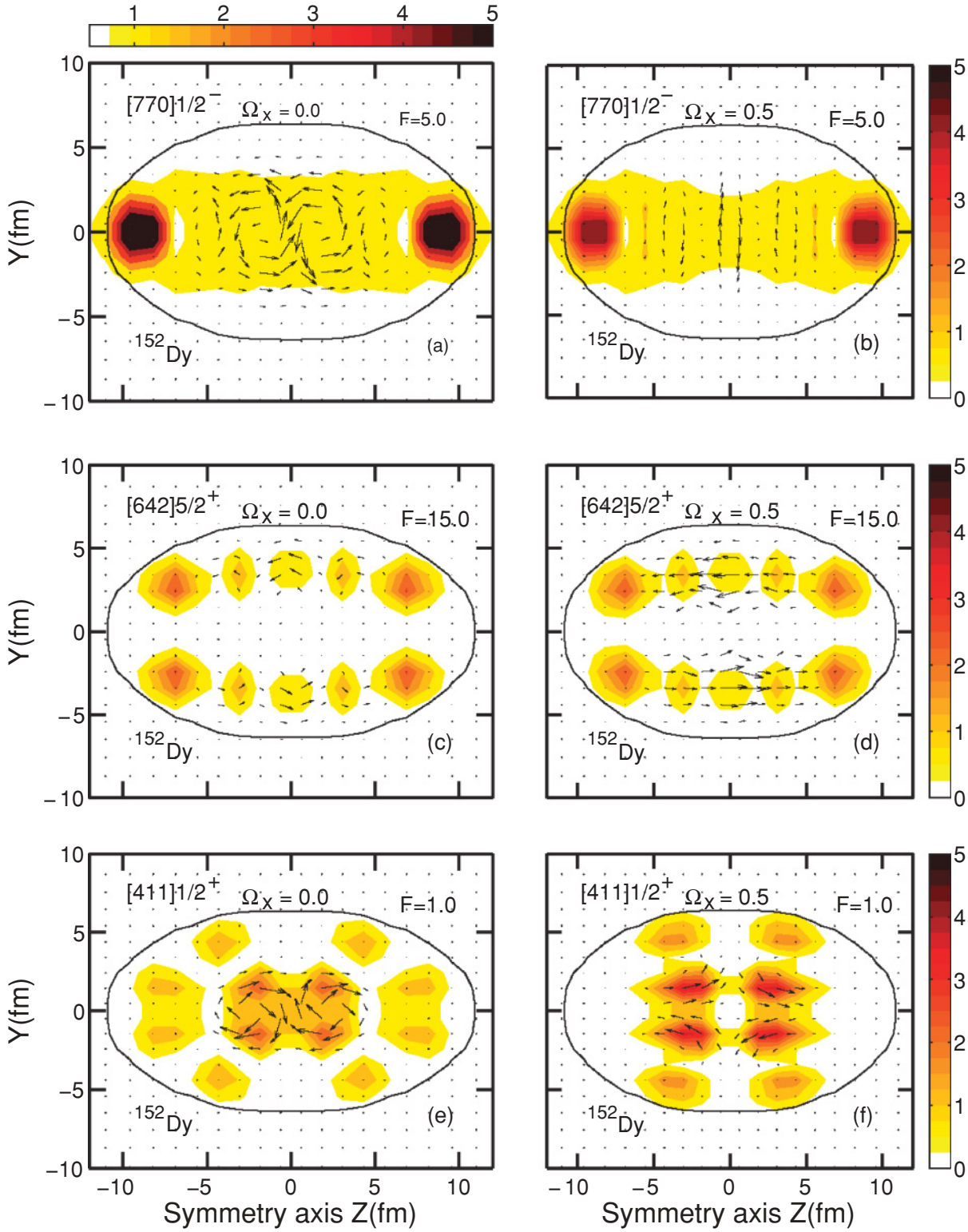

FIG. 9. (Color online) Current distributions $\boldsymbol{j}^n(\boldsymbol{r})$ produced by single neutron in indicated single-particle states of the yrast SD configuration in ^{152}Dy at rotational frequencies $\Omega_x = 0.0$ MeV (left panels) and $\Omega_x = 0.5$ MeV (right panels). The shape and size of the nucleus are indicated by density line which is plotted at $\rho = 0.01$ fm^{-3}. The currents in panels (e) and (f) are plotted at arbitrary units for better visualization. The currents in other panels are normalized to the currents in panels (e) and (f) by using the factor F. The currents and densities are shown in the intrinsic frame in the y-z plane at $x = 0.48$ fm. The single-neutron density distributions due to the occupation of the indicated Nilsson state are shown by the colormap. Note that slightly different colormap is used in panel (a) for better visualization of densities.

Even much large changes are induced by rotation into the structure of the $\nu[411]1/2^+$ state. The wave function in terms of two largest components has the $57\%[411]1/2+23\%[651]1/2$ and $84\%[411]1/2+13\%[411]3/2$ structure at $\Omega_x = 0.0$ MeV and $\Omega_x = 0.5$ MeV, respectively. One can see that the $\Delta N = 2$ interaction, leading to a considerable admixture of the $[651]1/2$ component into the structure of wave function, plays a very important role at no rotation. The change in the wave function induced by rotation leads to a considerable changes both in the nodal structure of density distribution and in the current distribution [compare Fig. 9(e) with Fig. 9(f)].

The wave function of the $\nu[770]1/2^-$ state is changed considerably by the rotation: Its structure in terms of two largest components is $62\%[770]1/2+17\%[761]1/2$ at $\Omega_x = 0.0$ MeV and $39\%[770]1/2+28\%[761]3/2$ and $\Omega_x = 0.5$ MeV. The increase of rotational frequency does not lead to appreciable modifications in the density distribution but considerably decreases the strength of the currents and changes the shape of the circulations [see Figs. 9(a) and 9(b). The latter is a consequence of additional Coriolis-induced currents. It is interesting that for this state the currents show maximum strength at the densities far below the maximum densities. This most likely explains relative weakness of the currents in this state as compared with those in the $\nu[411]1/2^+$ state. On the contrary, for many single-particle states the strongest currents are seen at or close to local increases in the densities [see Figs. 9(c), 9(d), 9(f), and 9(g) in the current article and Fig. 8 in Ref. [5]].

Our calculations show that the moments of inertia of the SD and HD configurations are very close to rigid-body values (Sec. IV). However, the intrinsic currents show the dramatic deviations from rigid rotation. Usually the deviations from the rigid-body moment of inertia imply that the flow pattern must substantially deviate from the current of a rigidly rotating mass distribution, i.e., there are strong net currents in the body-fixed frame [32]. However, the opposite is not true: the closeness of the moments of inertia to rigid-body value does not necessary imply that the current distribution should correspond to rigid rotation. On a microscopic level, the building blocks of the total current, namely the single-particle currents, certainly do not have a rigid-flow character; on the contrary, they have vortex-flow character (see Fig. 9).

Earlier nonrelativistic studies also point to the above-discussed relations between currents and rigid-body moments of inertia. For example, it was shown in Ref. [42] for the Schrödinger equation that single-valuedness requirement for the wave function implies nonexistence of rigid flow in a quantum fluid. Furthermore, it was demonstrated for a system of independent particles employing cranked harmonic oscillator potential that the current is not of the rigid-flow type even when the moment of inertia assumes the rigid-body value (Ref. [42]; see also Ref. [41]).

Current distributions shown in Figs. 8 and 9 are typical for collective rotation around the x axis perpendicular to the symmetry axis. Note that the alignment of the angular-momentum vector of a particle is specified along the x axis in the one-dimensional cranking approximation (see also discussion in Sec. IIIC of Ref. [5]). The $\Omega = 1/2$ orbitals are aligned with the axis of rotation (x axis) already at no rotation. As a result, the single-particle angular-momentum vector of the $\Omega = 1/2$ orbitals performs the precession around the x axis, thus orienting the currents predominantly in the y-z plane. In addition, the $\Omega = 1/2$ orbitals show vortices which are concentrated in the central region of nucleus. For the configurations with $\Omega \neq 1/2$, this mechanism of alignment becomes active only when the rotation sets up. Moreover, with increasing Ω, the densities and currents are pushed away from the axis of symmetry of the nucleus toward the surface area [Figs. 9(c) and 9(d) and Fig. 8 in Ref. [5]].

VI. FREQUENCY AND CONFIGURATION DEPENDENCIES OF THE IMPACT OF NUCLEAR MAGNETISM ON THE MOMENTS OF INERTIA

In this section, the frequency dependence of the impact of NM on the moments of inertia is studied using considerable number of SD and highly deformed configurations in ^{60}Zn obtained in unpaired CRMF calculations. The properties of yrast SD band in this nucleus were well described in this formalism above band crossing which takes place at $\Omega_x \sim 1$ MeV [11,46], while the CRHB + LN formalism gave a good description of this band in the band crossing region [31]. The neutron Routhian diagram for this configuration obtained in the calculations with the NLSH parametrization [48] is shown in Fig. 1 of Ref. [11]; the results with the NL1 parametrization are similar to the ones obtained with NLSH. All proton and neutron states below the $Z = 30$ and $N = 30$ SD shell gaps are occupied in this configuration (note that proton Routhian diagram is similar to the neutron one). The configurations are labeled by the shorthand notation $[n,p]$, where n (p) is the number of occupied $g_{9/2}$ neutrons (protons). In this notation, the yrast SD band has the [2,2] configuration. Excited configurations under consideration are built by means of proton or/and neutron particle-hole excitations across the $Z = 30$ and $N = 30$ SD shell gaps.

The results of calculations for contributions of NM into dynamic $[\Delta J^{(2)}_{\mathrm{NM-contr}}]$ and kinematic $[\Delta J^{(1)}_{\mathrm{NM-contr}}]$ moments of inertia are shown in Fig. 10. At low frequencies, the average contribution of NM into kinematic moment of inertia is slightly larger than 20% [Fig. 10(a)] and the $\Delta J^{(1)}_{\mathrm{NM-contr}}$ quantities show considerable dependence on configuration. The origin of the latter observation can be traced back to the specific features of some occupied single-particle orbitals. Let us consider as an example the [2,2] configuration. At low frequencies, the $\Delta J^{(1)}_{\mathrm{NM-contr}}$ values for this configuration are considerable higher than the $\Delta J^{(1)}_{\mathrm{NM-contr}}$ values averaged over all calculated configurations. This is due to the fact that upsloping branches of the proton and neutron $[440]1/2^+$ orbitals (in the $\Omega_x = 0.0$–0.7 MeV range, see Fig. 1 in Ref. [11]), characterized by the expectation values of the single-particle angular momentum $\langle \hat{j}_x \rangle_i$ strongly affected by NM, are occupied at $\Omega_x \leqslant 0.6$ MeV. At frequencies $\Omega_x \sim 0.8$ MeV, these orbitals strongly interact with proton and neutron $[431]3/2^+$ orbitals and exchange the character of the wave function. This leads to unpaired band crossing (see Ref. [11]) which is seen in considerable changes of $\Delta J^{(1)}_{\mathrm{NM-contr}}$

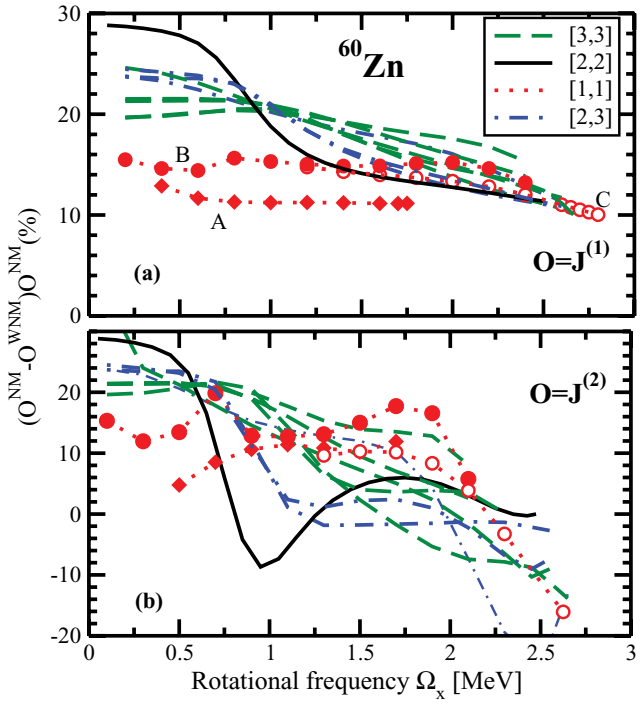

FIG. 10. (Color online) The contributions of NM to the dynamic [$J^{(2)}$] (b) and kinematic [$J^{(1)}$] (a) moments of inertia as a function of rotational frequency. Different color/line types are used for different groups of configurations characterized by the occupation of $g_{9/2}$ protons and neutrons.

and $\Delta J^{(2)}_{\mathrm{NM-contr}}$ quantities. The band crossing process is completed above $\Omega_x = 1.1$ MeV, where the orbital labeled as $[440]1/2^+$ is downsloping as a function of rotational frequency (see Fig. 1 in Ref. [11]). At these frequencies, the $\Delta J^{(1)}_{\mathrm{NM-contr}}$ quantity for the [2,2] configuration is slightly below the value of $\Delta J^{(1)}_{\mathrm{NM-contr}}$ averaged over all calculated configurations [Fig. 10(a)]. Note that this unpaired band crossing is not active in the [1] configurations because neither proton nor neutron $[440]1/2^+$ orbitals are occupied. The calculations also suggest that it is considerably suppressed in the [3,3] configurations due to the changes in the deformations and currents induced by the occupation of third $g_{9/2}$ orbital both in proton and neutron subsystems. However, the presence of this crossing is still visible [especially, in the $\Delta J^{(2)}_{\mathrm{NM-contr}}$ quantity] in some [2,3] configurations.

With increasing rotational frequency, the average contribution of NM into kinematic moments of inertia decreases and falls below 15% at $\Omega_x \sim 2.5$ MeV [Fig. 10(a)]. In addition, the configuration dependence of the $\Delta J^{(1)}_{\mathrm{NM-contr}}$ quantities is weaker than the one at low frequencies. At these frequencies, the majority of occupied single-particle orbitals are either completely aligned or very close to complete alignment. However, NM do not modify the expectation values of the single-particle angular momenta $\langle j_x \rangle_i$ of completely aligned orbitals [14]. As a result, only remaining orbitals, which are still aligning, contribute into $\Delta J^{(1)}_{\mathrm{NM-contr}}$. The combined contribution of these orbitals into $\Delta J^{(1)}_{\mathrm{NM-contr}}$ is smaller than the one at lower frequencies because the alignment of these orbitals is not far from complete.

The impact of NM on the dynamic moments of inertia is shown in Fig. 10(b) and it clearly displays much more complicated pattern as compared with the impact of NM on the kinematic moments of inertia. The irregularities in the $\Delta J^{(2)}_{\mathrm{NM-contr}}$ quantities are related to the band crossings. For example, the dip in the $\Delta J^{(2)}_{\mathrm{NM-contr}}$ values of the [2,2] configuration at $\Omega_x \sim 0.9$ MeV is caused by the unpaired band crossings which take place at different frequencies in the calculations with and without NM. Similar deviations from smooth trend as a function of rotational frequency are visible in other configurations. However, one can see that for some configurations the contribution of NM into dynamic moment of inertia is a smooth function of rotational frequency over extended frequency range. In this frequency range, the configurations remain unchanged. It is interesting that for some of these configurations the contributions of NM into dynamic moments of inertia are either close to zero or even negative; such features have not been seen in the previous analyses of the impact on time-odd mean fields on the dynamic moments of inertia [3,4,8,9].

The impact of NM on other physical observables of interest is shown in Fig. 11, in which the results of the NM and WNM calculations are compared as a function of total angular momentum. One can see that the quadrupole deformations β_2 [Fig. 11(a)] obtained in the calculations with and without NM differ by less than 3%. The only exception is configuration B, for which this difference reaches 7%. The difference in mass hexadecapole moments Q_{40} obtained in the calculations with and without NM is larger but typically below 10% [Fig. 11(c)]; the only exception is configuration B, for which this difference reaches 20% at $I \sim 20\hbar$. The γ deformations obtained in the calculations with and without NM differ by less than 1.5° [Fig. 11(b)]. The only significant difference is seen in the total binding energies [Fig. 11(d)], where the NM solution is more bound than the WNM solution. This effect, which is due to the modifications in the moments of inertia induced by NM, is very

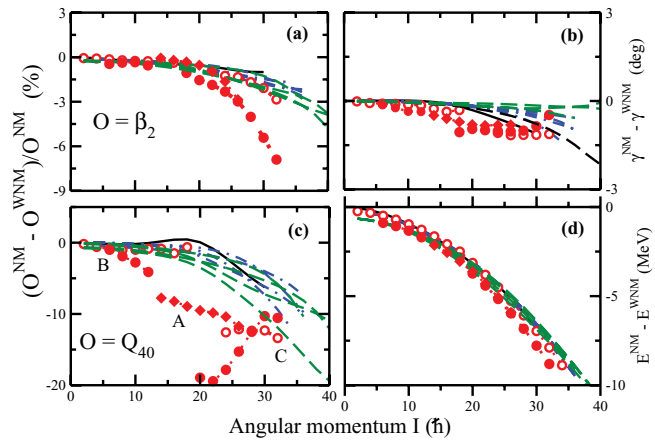

FIG. 11. (Color online) The contributions of NM to β_2 deformation (a), γ deformation (b), mass hexadecapole moment Q_{40} and total energy E (d) as a function of angular momentum I. Note that the results on panels (b) and (d) are shown in absolute values.

large: additional binding due to NM reaches 7–8 MeV at spin $I = 30\hbar$. These systematic results are consistent with the ones obtained in the previous studies of single SD configurations in ^{152}Dy [4] and single terminating configurations in ^{20}Ne [14]. They also give a hint why the cranked models based on the phenomenological potentials like Woods-Saxon or Nilsson, which do not include time-odd mean fields [3], are so successful in the description of experimental data. When considered as a function of spin the deformation properties of the rotating system are only weakly affected by time-odd mean fields, and the proper renormalization of the moments of inertia [26] takes care of the E versus angular-momentum curve.

VII. PARAMETRIZATION DEPENDENCE OF THE CONTRIBUTIONS OF NM TO THE MOMENTS OF INERTIA

It was shown in Ref. [5] that additional binding due to NM in one-particle states only weakly depends on the RMF parametrization; this is also seen in the analysis of terminating states in Ref. [14]. In this context, it is important to understand how the contributions of NM to the kinematic and dynamic moment of inertia depend on the RMF parametrization.

The dependence of the dynamic moments of inertia on the RMF parametrization has earlier been analyzed on the example of the SD bands in ^{151}Tb and ^{143}Eu in Ref. [10] and in ^{58}Cu and ^{60}Zn in Ref. [11] employing the NL1, NL3 [47], and NLSH [48] parametrizations of the RMF Lagrangian. The latter study includes also the results of calculations for kinematic moments of inertia. Additional calculations for these nuclei have also been performed with NL3* [33] and NLZ [49] parametrizations for the current article. As follows from these results, the kinematic and dynamic moments of inertia depend only weakly on the parametrization of the RMF Lagrangian. Indeed, at a given frequency all the results for kinematic (dynamic) moments of inertia fit into the window which have a width equal to approximately 5% (≈8%) [approximately 6% (≈10%)] of the value of kinematic (dynamic) moment of inertia in the $A \sim 150$ ($A \sim 60$) region of superdeformation. The larger spread of calculated values in the $A \sim 60$ mass region are most likely due to (i) larger softness of potential energy surfaces in these nuclei as compared with the ones in the $A \sim 150$ region of superdeformation and (ii) to larger relative importance of each particle and, thus, model uncertainties in the description of their single-particle energies.

Figure 12 shows the dependence of the contributions of NM to the kinematic and dynamic moments of inertia on the parametrization of the RMF Lagrangian. For simplicity of comparison, these quantities are normalized to those obtained in the calculations with the NL1 parametrization. Very weak dependence (within 5% window with respect of the NL1 results) of the contribution of NM to the kinematic moment of inertia on the RMF parametrization is seen in whole frequency range in ^{152}Dy [Fig. 12(c)] and at frequencies $\Omega_x \geqslant 0.75$ MeV in ^{60}Zn [Fig. 12(a)]. In the latter nucleus the deviation from the NL1 results reaches 10% at lower frequencies. The possible reasons for the larger dependence of calculated quantities on the parametrization in ^{60}Zn has been discussed above. On the other hand, the deviations from the NL1 results are larger for

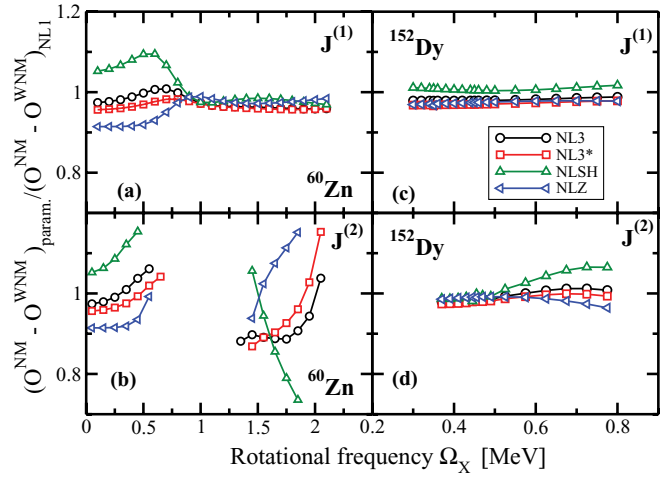

FIG. 12. (Color online) The contribution of NM to the physical observable O for specific parametrization of the RMF Lagrangian (the $[O^{NM} - O^{WNM}]_{param}$ quantity) normalized to the one obtained in the NL1 parametrization. The results of calculations are shown for yrast SD configurations in the ^{60}Zn and ^{152}Dy nuclei. Note that band crossing region is excluded in (b).

the dynamic moments of inertia. These deviations can be as large as 8% at highest frequencies in the yrast SD configuration of ^{152}Dy [Fig. 12(d)] and as large as 20% in the yrast SD configuration in ^{60}Zn [Fig. 12(b)]. Considering that the dynamic moment of inertia is related to the second derivative of the total energy with respect of spin, a larger dependence of the dynamic moment of inertia on the parametrization is expected.

These values can be used to estimate the uncertainty in the definition of the moments of inertia in the CRMF calculations due to the uncertainty in NM. The latter is related to the dependence of the $[O^{NM} - O^{WNM}]_{param}$ quantities (Fig. 12) on the RMF parametrization discussed above. Dependent on nuclear system and configuration, the NM contribution to the total kinematic and dynamic moments of inertia is approximately 10–25% (Secs. IV and VI). Thus, the uncertainty of the definition of the absolute value of the total dynamic and kinematic moments of inertia due to the uncertainty in the definition of NM is modest, being in the range of 0.5–5.0%. The fact that the moments of inertia of rotational bands of different structure in the unpaired regime are well described (typically within 5% of experimental data [1,9–12,50]) in the CRMF calculations strongly suggests that NM and its impact on the moments of inertia is reasonably well defined in the CDFT theory.

VIII. TERMINATING STATES

The majority of rotational bands which do not have large deformation at spin zero will terminate in a noncollective terminating state at I_{max} [26,51,52].[3] The regime of nuclear

[3]Only recently the evidences for nontermination of some rotational bands at I_{max} have been found [53].

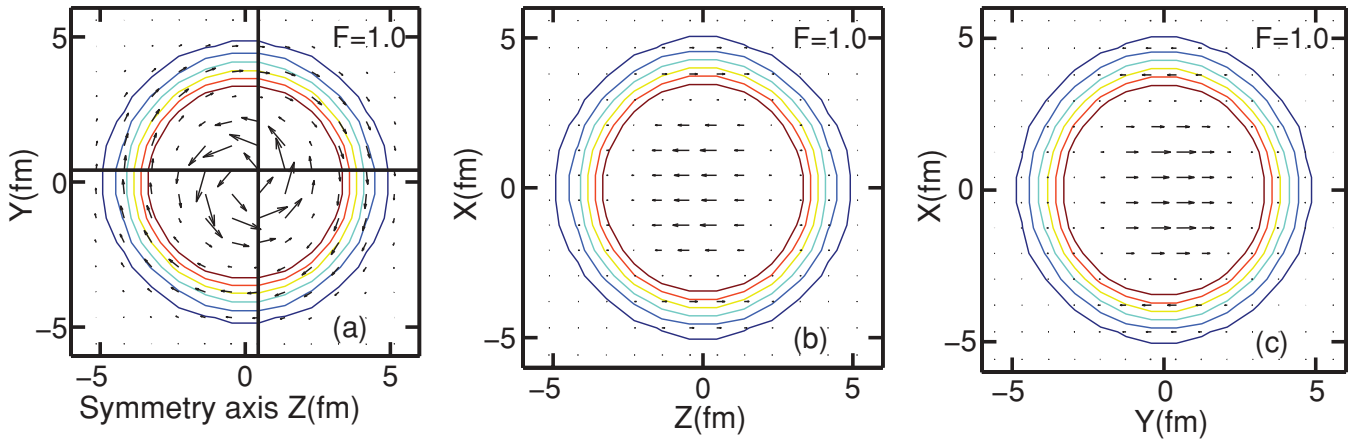

FIG. 13. (Color online) Neutron current distributions $\boldsymbol{j}^n(\boldsymbol{r})$ in the intrinsic frame in the y-z plane (at $x = 0.416$ fm) (left panel), in the x-z plane (at $y = 0.416$ fm) (middle panel), and in the x-y plane (at $z = 0.457$ fm). These distributions are shown for the state of ^{47}V terminating at $I = 17.5^+$. The currents are plotted at arbitrary units for better visualization. The shape and size of the nucleus are indicated by density lines which are plotted in the range 0.01–0.06 fm^{-3} in increments of 0.01 fm^{-3}. The vertical and horizontal lines in the left panel show the cross sections at which the currents in the z-x plane (middle panel) and in the y-x plane (right panel) are plotted, respectively.

motion in terminating state is usually referred as "non-collective rotation" [26,54]. This is because of the fact that for an axially symmetric potential, the nucleon orbitals are not influenced by the rotation around the symmetry axis of this potential; thus, collective rotation about that axis is not possible. Non-collective rotation is also realized in the aligned states such as "yrast traps" (or "yrast isomers") [55–57]. The study of terminating states in the context of understanding of time-odd mean fields is of considerable interest because of several reasons. First, time-odd mean fields provide an additional binding to the energies of the specific configuration, and this additional binding increases with spin and has its maximum exactly at the terminating state [14]. This suggests that the terminating states can be an interesting probe of time-odd mean fields [14,27,58] provided that other effects can be reliably isolated [14]. Second, at the band termination, the NM does not modify either total angular momentum or the expectation values of the single-particle angular momenta $\langle \hat{j}_x \rangle_i$ [14]. Third, terminating state is a (multi-)particle + (multi-)hole noncollective state in which the angular momenta of all particles and holes outside the core are aligned along the symmetry axis.

We will consider in this section the $\pi(d_{3/2})^{-1}_{1.5}(f_{7/2})^4_8 \otimes \nu(f_{7/2})^4_8$ terminating state in ^{47}V, which has $I_{\max} = 17.5^+$, as an example. The structure of this state is given with respect of the ^{40}Ca core. This state is characterized by the largest impact of NM on the binding energies among terminating states studied in Ref. [14]. It is nearly spherical with the quadrupole deformation $\beta_2 \sim 0.03$ (Fig. 6 in Ref. [14]). Our goal is to understand the impact of NM on the current distribution and microscopic origin of additional binding due to NM.

In terminating states, the angular momenta of valence particles and holes are aligned along the symmetry axis (x axis). As a consequence they perform precession around this axis, generating azimuthal currents with respect to the symmetry axis. This is illustrated in Fig. 13. One can see two azimuthal circulations in the y-z plane: the circulation in the central region of nucleus is directed counterclockwise while the one in the surface region is directed clockwise. Figure 14 shows total (left panel), Coriolis-induced (middle panel), and magnetic potential–induced (right panel) currents. One can see that surface circulation is generated by the Coriolis term, while the central circulation by the magnetic potential. The currents in the x-z and x-y planes are perpendicular to the x axis (Fig. 13). This clearly shows that the currents are azimuthal.

In Ref. [5], the polarization effects induced by NM have been investigated in one- and two-particle configurations of odd and odd-odd nonrotating nuclei. Terminating states differ significantly from these configurations. First, they are multiparticle+multihole configurations. For example, the $\pi(d_{3/2})^{-1}_{1.5}(f_{7/2})^4_8 \otimes \nu(f_{7/2})^4_8$ terminating state in ^{47}V has eight particles and one hole outside the ^{40}Ca core. Second, the alignment of the angular momenta of these particles and holes generates considerable total angular momentum ($I = 17.5\hbar$ in the discussed terminating state of ^{47}V) aligned along the axis of symmetry; this momentum is much larger than the one in odd and odd-odd nuclei studied in Ref. [5]. Third, terminating states are characterized by the azimuthal currents with respect to the symmetry axis, while the states in nonrotating nuclei are characterized by the currents shown in Figs. 7-9 of Ref. [5]. Thus, it is interesting to see how these differences affect the polarization effects induced by NM and whether these polarization effects are similar in nature for these two classes of noncollective states, namely low-spin one- and two-particle configurations of nonrotating nuclei and high-spin terminating states.

In order to facilitate the discussion, we split the total energy of the system (Refs. [6,9]) into different terms as[4]

$$E_{\rm tot} = E_{\rm part} + E_{\rm Cor} + E_{\rm c.m.} - E_\sigma - E_{\sigma\rm NL} - E^{\rm TL}_\omega - E^{\rm TL}_\rho - E^{\rm SL}_\omega - E^{\rm SL}_\rho - E_{\rm Coul}, \quad (22)$$

[4]We follow Refs. [5,59] in the selection of the signs of the energy terms.

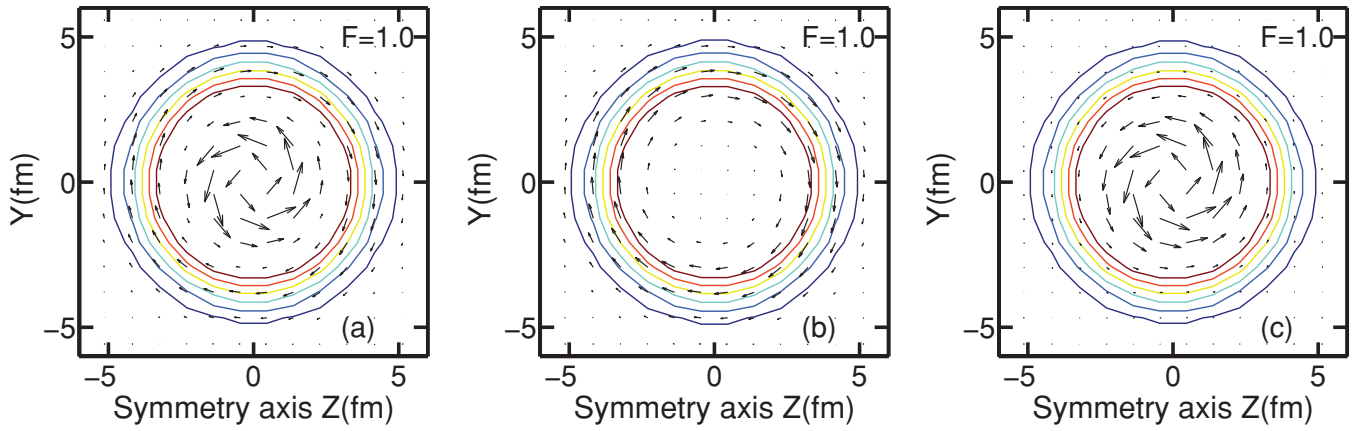

FIG. 14. (Color online) Neutron current distributions $\boldsymbol{j}^n(\boldsymbol{r})$ in the intrinsic frame in the y-z plane (at $x = 0.407$ fm). These distributions are shown for the state of ^{47}V terminating at $I = 17.5^+$. The left, middle, and right panels show total, Coriolis-induced, and magnetic potential–induced currents, respectively. See the caption for Fig. 13 for other details.

where $E_{\rm part}$, $E_{\rm Cor}$, and $E_{\rm c.m.}$ represent the contributions from fermionic degrees of freedom, whereas the other terms are related to mesonic (bosonic) degrees of freedom. In Eq. (22)

$$E_{\rm part} = \sum_i^A \varepsilon_i \tag{23}$$

is the energy of the particles moving in the field created by the mesons (ε_i is the energy of i-th particle and the sum runs over all occupied proton and neutron states),

$$E_{\rm Cor} = \Omega_x \sum_i^A \langle i|\hat{j}_x|i\rangle \tag{24}$$

is the energy of the Coriolis term,

$$E_\sigma = \frac{1}{2} g_\sigma \int d^3r \sigma(\boldsymbol{r}) \left[\rho_s^p(\boldsymbol{r}) + \rho_s^n(\boldsymbol{r})\right] \tag{25}$$

is the linear contribution to the energy of isoscalar-scalar σ field,

$$E_{\sigma\rm NL} = \frac{1}{2} \int d^3r \left[\frac{1}{3} g_2 \sigma^3(\boldsymbol{r}) + \frac{1}{2} g_3 \sigma^4(\boldsymbol{r})\right] \tag{26}$$

is the nonlinear contribution to the energy of isoscalar-scalar σ field,

$$E_\omega^{\rm TL} = \frac{1}{2} g_\omega \int d^3r \omega_0(\boldsymbol{r}) \left[\rho_v^p(\boldsymbol{r}) + \rho_v^n(\boldsymbol{r})\right] \tag{27}$$

is the energy of the time-like component of isoscalar-vector ω field,

$$E_\rho^{\rm TL} = \frac{1}{2} g_\rho \int d^3r \rho_0(\boldsymbol{r}) \left[\rho_v^n(\boldsymbol{r}) - \rho_v^p(\boldsymbol{r})\right] \tag{28}$$

is the energy of the time-like component of isovector-vector ρ field,

$$E_\omega^{\rm SL} = -\frac{1}{2} g_\omega \int d^3r \boldsymbol{\omega}(\boldsymbol{r}) [\boldsymbol{j}^p(\boldsymbol{r}) + \boldsymbol{j}^n(\boldsymbol{r})] \tag{29}$$

is the energy of the space-like component of isoscalar-vector ω field,

$$E_\rho^{\rm SL} = -\frac{1}{2} g_\rho \int d^3r \boldsymbol{\rho}(\boldsymbol{r}) [\boldsymbol{j}^n(\boldsymbol{r}) - \boldsymbol{j}^p(\boldsymbol{r})] \tag{30}$$

is the energy of the space-like component of isovector-vector ρ field,

$$E_{\rm Coul} = \frac{1}{2} e \int d^3r A_0(\boldsymbol{r}) \rho_v^p(\boldsymbol{r}) \tag{31}$$

is the Coulomb energy, and

$$E_{\rm c.m.} = -\tfrac{3}{4}\hbar\omega_0 = -\tfrac{3}{4} 41 A^{-1/3} {\rm MeV} \tag{32}$$

is the correction for the spurious center-of-mass motion approximated by its value in a nonrelativistic harmonic oscillator potential.

Polarization effects induced by NM are investigated by considering NM impact on different terms of the total energy [Eq. (22)]. The results of this study are shown in Table I. Similarly to Ref. [5], the $E_\rho^{\rm TL}$ and $E_\rho^{\rm SL}$ terms are only weakly influenced by NM, and, thus, they will not be discussed in detail. A somewhat stronger impact of NM is seen in the $E_{\rm Coul}$, $E_{\sigma\rm NL}$, and $E_\omega^{\rm SL}$ terms. Note that only last term was appreciably affected in low-spin configurations of odd and odd-odd nuclei in Ref. [5]. Much larger polarization effects are seen in the $E_{\rm part}$, E_σ, and $E_\omega^{\rm TL}$ terms. The E_σ and $E_\omega^{\rm TL}$ terms depend only indirectly on time-odd mean fields through the polarizations of time-even mean fields induced by NM [5]. One should keep in mind that only the $E_\sigma + E_\omega^{\rm TL}$ quantity has a deep physical meaning, as it defines a nucleonic potential; this sum is modified by NM on −5.9 MeV.

Comparing these results with those presented in Ref. [5], one can conclude that polarization effects for different total-energy terms in the terminating state under study are stronger by at least one order of magnitude than in low-spin one- and two-particle configurations of nonrotating nuclei. This is a consequence of the fact that all particles (eight) and holes (one) outside the ^{40}Ca core participate in building the total angular momentum and currents in the terminating state, while only one (two) particle(s) participate in generating the currents in

TABLE I. Impact of NM on different terms of the total energy [Eq. (22)] in the state of ^{47}V terminating at $I = 17.5^{+}$. Column 2 shows the absolute energies (in MeV) of different energy terms in the case when NM is neglected. Columns 3 and 4 list the changes $\Delta E_i = E_i^{\rm NM} - E_i^{\rm WNM}$ (in MeV) in the energies of these terms induced by NM in self-consistent (column 3) and perturbative (column 4) calculations. Note that only nonzero quantities are listed in column 4. The results of calculations are obtained at rotational frequency $\Omega_x = 2.4$ MeV. The energies of the Coriolis term $E_{\rm Cor}$ and particle energy $E_{\rm part}$ depend on frequency. The latter takes place through the modifications of the energies of single-particle states with frequency (see, for example, Sec. 3.8 and Fig. 6a in Ref. [26] for more details on a construction of terminating state). However, the sum $E_{\rm Cor} + E_{\rm part}$ does not depend on frequency. Other remaining quantities shown in column 1 and the ΔE_i quantities shown in columns 3 and 4 are frequency independent.

Quantity 1	$E_i^{\rm WNM}$ 2	ΔE_i 3	$\Delta E_i^{\rm pert}$ 4
$E_{\rm part}$	−1217.668	−15.5	−7.296
$E_{\rm Cor}$	42.0	0	
E_σ	−6381.875	−85.231	
$E_{\sigma\rm NL}$	109.368	−2.815	
$E_\omega^{\rm TL}$	5371.721	79.291	
$E_\omega^{\rm SL}$	0.0	−3.51	−3.51
$E_\rho^{\rm TL}$	0.549	−0.002	
$E_\rho^{\rm SL}$	0.0	−0.038	−0.038
$E_{\rm Coul}$	102.168	0.515	0.240
$E_{\rm c.m.}$	−8.521	0.0	
$E_{\rm tot}$	−386.121	−3.704	−3.983

nonrotating odd (odd-odd) nuclei [5]. Despite this, the relative impact of NM on different terms of the total energy is, in general, similar in these two classes of noncollective states (compare Table I in the present article with Tables I, II, and IV in Ref. [5]).

Total modifications of the energies due to NM in the mesonic sector are −11.79 MeV. Only one-third of these modifications comes from the terms ($E_\omega^{\rm SL}$, $E_\omega^{\rm SL}$) which directly depend on nucleonic currents, whereas the rest are from the modifications of time-even mean fields induced by NM.

It is interesting to compare the results of self-consistent and perturbative calculations.[5] The $\Delta E_i^{\rm pert} = E_i^{\rm NM} - E_i^{\rm WNM}$ quantities will be used for simplicity in further discussion. These quantities are shown in columns 3 and 4 of Table I. The ΔE_σ, $\Delta E_{\sigma\rm NL}$, $\Delta E_\omega^{\rm TL}$, and $\Delta E_\rho^{\rm TL}$ quantities are zero in perturbative calculations because time-even fields are fixed in these calculations. The $\Delta E_\omega^{\rm SL}$ and $\Delta E_\rho^{\rm SL}$ are the same in self-consistent (column 3) and perturbative (column 4) calculations because the $E_\omega^{\rm TL}$ and $E_\rho^{\rm TL}$ terms depend only on time-odd mean fields, which are the same in the parts of the calculations that include NM. Particle energies $E_{\rm part}$ are strongly modified by NM in self-consistent calculations; they change by −15.5 MeV. Perturbative calculations show that only one half of $\Delta E_{\rm part}$ is coming directly from time-odd mean fields (see Sec. IVB of Ref. [5] for more details on this mechanism); the rest is due to polarization effects in time-even fields induced by NM. The same is true for the Coulomb energy term $E_{\rm Coul}$.

It is evident from Table I that

$$\Delta E_{\rm tot}^{\rm self-const} \approx \Delta E_{\rm tot}^{\rm pert}. \quad (33)$$

Note that the superscripts self-const and pert refer to fully self-consistent and perturbative results. The analysis of polarization effects in other terminating states of the $A \sim 40$ mass region shows the same relation. These results clearly indicate that the additional binding due NM (the $E^{\rm NM} - E^{\rm WNM}$ quantity) is defined mainly by time-odd fields and that the polarization effects in fermionic and mesonic sectors of the model cancel each other to a large degree. The same result has been earlier obtained in the analysis of nonrotating nuclei in Ref. [5].

IX. SIGNATURE-SEPARATED CONFIGURATIONS

Signature separation phenomenon induced by time-odd mean fields has been found earlier in excited four-particle SD configurations of ^{32}S [31,60] and, very recently, in two-particle configurations of nonrotating odd-odd nuclei in Ref. [5]. It reveals itself in a considerable energy splitting of the $r_{\rm tot} = +1$ and $r_{\rm tot} = -1$ branches of the configurations which have the same structure in terms of occupation of single-particle states with given Nilsson labels. Such a signature separation could not have been obtained in phenomenological cranking models, such as the ones using the Woods-Saxon or Nilsson potentials, since time-odd mean fields are absent in these models.

However, the description of rotating $N \approx Z$ nuclei requires isospin projection [61] which can modify above mentioned results. Since this projection is beyond the current framework, we concentrate at the nuclei away from the $N = Z$ line. The analysis of Ref. [5] shows that signature separation is expected also in such nuclei, but it is weaker as compared with the one seen in the nuclei around the $N = Z$ line. Unfortunately, the survey of odd-odd $A = 20$–52 nuclei (some of which were studied in Ref. [5]) does not reveal experimental bands in the nuclei away from the $N = Z$ line in which signature separation is expected.

Figure 15 shows that signature separation phenomenon can also be present in heavier nuclei. This figure shows the results of calculations for odd-odd Eu isotopes in which odd proton occupies fixed $\pi[532]5/2^+$ state, and odd neutron occupies different neutron states of the $r = \pm i$ signatures along the isotope chain. Additional binding due to NM (the $E^{\rm NM} - E^{\rm WNM}$ quantity, see Ref. [5] for more details) is shown for total

[5]Fully self-consistent calculations with NM provide a starting point for perturbative calculations. Using their fields as input fields, only one iteration is performed in the calculations without NM: this provides perturbative results. Time-even mean fields are the same in both (fully self-consistent and perturbative) calculations. Then, the impact of time-odd mean fields on calculated quantities (for example, different terms in the total energy [Eq. (22)] is defined as the difference between the values of this quantity obtained in these two calculations. In this way, the pure effects of time-odd mean fields in fermionic and mesonic channels of the model are isolated because no polarization effects are introduced into time-even mean fields [5].

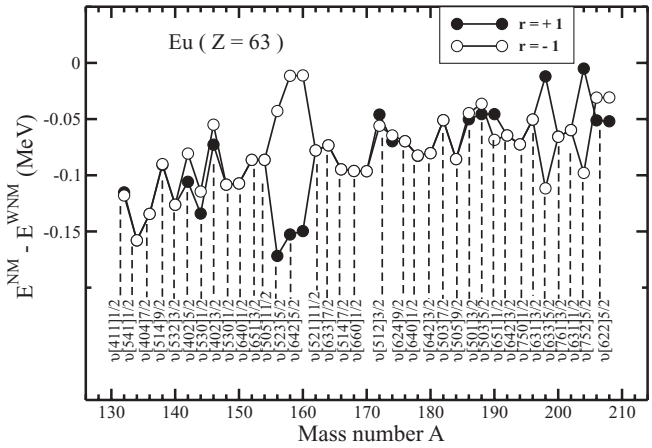

FIG. 15. The impact of NM on binding energies of the configurations in odd-odd Eu ($Z = 63$) nuclei at $\Omega_x = 0.0$ MeV. The $E^{\rm NM} - E^{\rm WNM}$ quantity is shown for different total signatures r. Proton configuration has blocked $\pi[532]5/2^+$ state for all isotopes, while the neutron configuration changes as a function of mass number. Configurations are labeled with the Nilsson labels of blocked odd neutron state; configurations at and to the right of the Nilsson label up to the next Nilsson label have the same blocked neutron state.

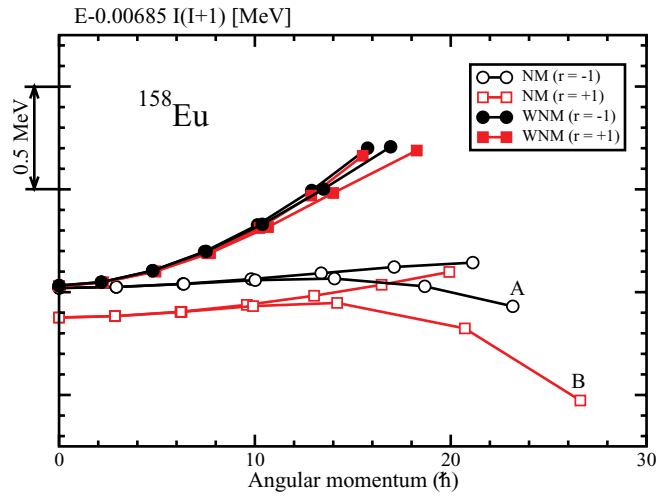

FIG. 16. (Color online) The energies of calculated bands in ^{158}Eu based on the $\pi[532]5/2^{\pm} \otimes \nu[642]5/2^{\pm}$ two-particle configurations as a function of angular momentum with rigid rotor reference subtracted. The results of the calculations with and without NM are shown.

proton-neutron configurations with different total signatures $r_{\rm tot} = \pm i$. Significant signature separation (on the level of 100–150 keV) is seen in the $\pi[532]5/2 \otimes \nu[523]5/2$ (^{156}Eu), $\pi[532]5/2 \otimes \nu[642]5/2$ (^{158,160}Eu), $\pi[532]5/2 \otimes \nu[633]5/2$ (^{196}Eu), and $\pi[523]5/2 \otimes \nu[752]5/2$ (^{204}Eu) configurations. Either $r = -1$ or $r = +1$ states can be more bound in signature separated configurations of Eu isotopes (Fig. 15). This depends on mutual orientation of proton and neutron currents induced by odd proton and odd neutron; the state with the same orientation of these currents is more bound.

Figure 16 illustrates that four rotational sequences (two with total signature $r_{\rm tot} = +1$ and two with $r_{\rm tot} = -1$) can be built in the two-particle configurations $\pi|a\rangle(r = \pm i) \otimes \nu|b\rangle(r = \pm i)$ (where $|a\rangle$ and $|b\rangle$ indicate the blocked proton and neutron Nilsson states, respectively) of odd-odd nuclei. For the case of ^{158}Eu we consider two-particle configurations based on the $|a\rangle = [532]5/2$ and $|b\rangle = [642]5/2$ states. In the WNM calculations, the $r_{\rm tot} = +1$ and $r_{\rm tot} = -1$ configurations are almost degenerate in energy up to spin $I \sim 10\hbar$ (Fig. 16). On the contrary, there is a considerable signature separation ($\approx$150 keV) due to time-odd mean fields between these configurations in the calculations with NM. This feature is a strong spectroscopic fingerprint of the presence of time-odd mean fields. Note that rotational sequences A and B undergo unpaired band crossings at $I \sim 20\hbar$.

Unfortunately, the experimental data on odd-odd Eu nuclei also do not reveal the configurations discussed above in which the signature separation is expected. This situation may be resolved by a systematic search of signature separated configurations both in the experimental data on odd-odd rare-earth nuclei and in the model calculations. The best way to confirm the existence of this phenomenon would be to find in model calculations the configurations of odd-odd nuclei which show no signature splitting in the absence of time-odd mean fields and measurable signature separation in the presence of time-odd mean fields and then to find their experimental counterparts which show signature separation. However, such an investigation is definitely beyond the scope of the current study. The difficulty of such a study is also underlined by the fact that existing interpretations of two-quasiparticle configurations in odd-odd nuclei are based on Woods-Saxon or Nilsson potentials. In these potentials, the signature degeneracy is considered to be a strong fingerprint of specific configurations. However, time-odd mean fields in EDF provide additional mechanism of breaking the signature degeneracy, so the experimental data on such configurations has to be reanalyzed in density functional calculations.

Although the model calculations clearly indicate the important role of time-odd mean fields in creating signature separation phenomenon in odd-odd nuclei, the direct comparison with experiment will be complicated by the number of model limitations which are related to (a) the presence of residual proton-neutron interaction of unpaired proton and neutron and (b) the coupling scheme of angular momenta vectors of unpaired proton and neutron at low spin.

In odd-odd nuclei the angular momenta of unpaired proton and unpaired neutron in two-quasiparticle configurations can be coupled either in parallel or antiparallel fashion, namely into $K_> = \Omega_p + \Omega_n$, and $K_< = |\Omega_p - \Omega_n|$, where $\Omega_{p(n)}$ represents the projection of single quasiparticle angular momentum of proton (neutron) on the axis of symmetry. For example, in ^{158}Eu this will lead to rotational sequences with $K_< = 0$ and $K_> = 5$. The degeneracy of the bandheads of the $K_{><}$ doublet pair (called Gallagher-Moszkowski doublet [62]) is lifted by inclusion of the residual proton-neutron interaction and also by the zero-point rotational energy. Relative energy ordering of the $K_>$ and $K_<$ bands is determined by the empirical Gallagher-Moszkowski (GM) rule which places the spin-parallel band lower in energy than its spin-antiparallel counterpart [62] in odd-odd nuclei (and vice versa in even-even nuclei

[63]) and has only few exceptions [64,65]. Another important consequence of the residual interaction of unpaired nucleons is the observed shift of the odd- and even-spin rotational levels relative to each other in the $K = 0$ bands; this feature is generally referred to as the Newby or odd-even shift [66].

Residual proton-neutron interaction of unpaired nucleons is neglected in the cranking models; we are not aware of any publication which includes it. So neither Gallagher-Moszkowski splittings nor Newby shifts can be described in the current calculations. It is also necessary to recognize that two-quasiparticle configurations in odd-odd and even-even nuclei show a daunting complexity due to the high density of states and the large number of couplings and interactions possible. The problem of the description of the Gallagher-Moszkowski splittings and Newby shifts is far from being settled even in the framework of conventional particle + rotor model [63–65,67,68]. For example, the residual interaction of unpaired proton and neutron in odd-odd nuclei shows pronounced dependence on the mass region under study [64,65]. It is even more difficult to understand why in two-quasiparticle configurations of the rare-earth region different residual interactions are required to describe the interaction between unpaired proton and neutron in odd-odd nuclei and between unpaired protons (neutrons) in even-even nuclei [63] despite the expectations that they should be the same due to isospin symmetry. To our knowledge, a self-consistent description of Gallagher-Moszkowski splittings and Newby shifts has been attempted only in the framework of the rotor + two-quasiparticle model based on Skyrme Hartree + Fock approach in Ref. [69].

At zero rotational frequency the angular momenta of odd proton and odd neutron are aligned (parallel or antiparallel) with the symmetry axis which leads to bandhead states with $K_> = \Omega_p + \Omega_n$ and $K_< = |\Omega_p - \Omega_n|$. However, in one-dimensional cranking approximation nuclear configuration on top of which rotational sequence is built does not depend on coupling of Ω_p and Ω_n. This is a well-known (although seldom stressed) deficiency of the one-dimensional cranking approximation. However, with increasing rotational frequency the angular momenta of odd protons and odd neutrons start to align with the axis of rotation, which is perpendicular to the axis of symmetry. Although it is tempting to employ the tilted axis cranking (TAC) approximation for the description of the combination of these two angular-momenta coupling schemes at low spin, this does not resolve the problem of the description of signature separation since signature is no longer a good quantum number in the TAC approximation [70]. On the contrary, the one-dimensional cranking approximation used in the current article has a clear advantage that it properly accounts for the alignments of valence particles and holes along the axis of rotation at medium and high spins where $I \geqslant K$ [57] and thus provides correct description of signature separation at these spins.

X. CONCLUSIONS

Time-odd mean fields (nuclear magnetism) have been studied in rotating nuclei in a systematic way within the framework of CDFT. The main results can be summarized as follows:

(i) NM can considerably modify the band crossing features (crossing frequencies and the properties of kinematic and dynamic moments of inertia in the band crossing region). In the calculations without pairing, these modifications depend on the underlying changes in the single-particle properties such as alignments and energies induced by NM. These effects are also active in the calculations with pairing. In addition, in the calculations with pairing the gradual breaking of high-j pairs proceeds faster in the presence of NM, which is reflected in a faster decrease of pairing with increasing Ω_x. Thus we can specify this effect as an antipairing effect induced by NM.

(ii) Outside the band crossing regions, the contribution of NM to the kinematic and dynamic moments of inertia only weakly depends on the RMF parametrization.

(iii) It is shown for the first time within the self-consistent approach that the moments of inertia of super- and hyperdeformed configurations in unpaired regime come very close to the rigid-body values. Despite this, the presence of strong vortices demonstrates the dramatic deviation of the currents from rigid rotation. On the contrary, the moments of inertia of normal-deformed nuclei deviate considerably from the rigid-body value in the calculations without pairing.

(iv) The complicated structure of the currents in the rotating systems of independent fermions is the consequence of the fact that total current is the sum of the single-particle currents. The single-particle currents show vortices (circulations), the strength and localization of which depend on the single-particle state.

(v) Within specific configuration the impact of NM on the binding energies reaches its maximum at the terminating state [14]. Underlying microscopic mechanism for additional binding due to NM at such states has the same features as those seen in low-spin one- and two-particle configurations of odd and odd-odd nuclei [5]. However, the magnitude of the effects is significantly larger. The perturbative results clearly indicate that additional binding due NM at terminating states is defined mainly by time-odd fields and that the polarization effects in fermionic and mesonic sectors of the model cancel each other to a large degree.

(vi) The signature-separation phenomenon in odd-odd nuclei has been analyzed in detail. It is shown that the effects neglected in the current approach, such as the residual interaction of unpaired protons and neutrons and the coupling scheme of angular-momenta vectors of these particles at low spin, considerably complicate the quantitative description of the spectra of odd-odd nuclei. The best way to confirm the existence of this phenomenon would be to find (both in experiment and in calculations) the configurations of odd-odd nuclei which show no signature splitting in the absence of time-odd mean fields and measurable signature separation in the presence of time-odd mean fields.

Although time-odd mean fields affect different physical observables (see the Introduction in Ref. [5] for details), this investigation clearly shows that rotating nuclei still offer one of the best probes of this channel of density functional theories. This is because the impact of time-odd mean fields is significant, representing on average 20% of kinematic and dynamic moments of inertia. In addition, it shows appreciable variations with configuration, particle number, and rotational frequency; these variations provide a useful tool for a better test or definition of time-odd mean fields. A significant amount of the data on different types (normal- [12], superdeformed [1,9–11,35,71], and smooth terminating [1,26]) of rotational bands in an unpaired regime available in different mass regions offers a testing ground for time-odd mean fields. These data are also extremely useful for fitting the parameters of time-odd mean fields as needed, for example, in Skyrme energy density functionals, in which these fields are not well defined (Refs. [3,29]). Our investigation, however, suggests that such fit has to be performed to a significant set of rotational structures representing different mass regions and different configurations and spanned over significant frequency range in order to minimize the dependence of the fit parameters on the choice of experimental data.

ACKNOWLEDGMENTS

The material is based on work supported by the Department of Energy under Grant No. DE-FG02-07ER41459.

[1] D. Vretenar, A. V. Afanasjev, G. A. Lalazissis, and P. Ring, Phys. Rep. **409**, 101 (2005).
[2] M. Bender, P.-H. Heenen, and P.-G. Reinhard, Rev. Mod. Phys. **75**, 121 (2003).
[3] J. Dobaczewski and J. Dudek, Phys. Rev. C **52**, 1827 (1995).
[4] A. V. Afanasjev and P. Ring, Phys. Rev. C **62**, 031302(R) (2000).
[5] A. V. Afanasjev and H. Abusara, Phys. Rev. C **81**, 014309 (2010).
[6] W. Koepf and P. Ring, Nucl. Phys. A **493**, 61 (1989).
[7] U. Post, E. Wüst, and U. Mosel, Nucl. Phys. A **437**, 274 (1985).
[8] J. König and P. Ring, Phys. Rev. Lett. **71**, 3079 (1993).
[9] A. V. Afanasjev, J. König, and P. Ring, Nucl. Phys. A **608**, 107 (1996).
[10] A. V. Afanasjev, G. Lalazissis, and P. Ring, Nucl. Phys. A **634**, 395 (1998).
[11] A. V. Afanasjev, I. Ragnarsson, and P. Ring, Phys. Rev. C **59**, 3166 (1999).
[12] A. V. Afanasjev and S. Frauendorf, Phys. Rev. C **71**, 064318 (2005).
[13] A. V. Afanasjev, P. Ring, and J. König, Nucl. Phys. A **676**, 196 (2000).
[14] A. V. Afanasjev, Phys. Rev. C **78**, 054303 (2008).
[15] H. Abusara and A. V. Afanasjev, Phys. Rev. C **79**, 024317 (2009).
[16] M. Matev, A. V. Afanasjev, J. Dobaczewski, G. A. Lalazissis, and W. Nazarewicz, Phys. Rev. C **76**, 034304 (2007).
[17] A. V. Afanasjev, T. L. Khoo, S. Frauendorf, G. A. Lalazissis, and I. Ahmad, Phys. Rev. C **67**, 024309 (2003).
[18] A. V. Afanasjev and H. Abusara, Phys. Rev. C **78**, 014315 (2008).
[19] D. R. Inglis, Phys. Rev. **96**, 1059 (1954).
[20] B. B. Serot and J. D. Walecka, Adv. Nucl. Phys. **16**, 1 (1986).
[21] P.-G. Reinhard, M. Rufa, J. Maruhn, W. Greiner, and J. Friedrich, Z. Phys. A **323**, 13 (1986).
[22] M. Yamagami and K. Matsuyanagi, Nucl. Phys. A **672**, 123 (2000).
[23] B. G. Carlsson, J. Dobaczewski, and M. Kortelainen, Phys. Rev. C **78**, 044326 (2008).
[24] J. Dobaczewski, B. G. Carlsson, and M. Kortelainen, J. Phys. G **37**, 075106 (2010).
[25] W. Negele, in *Effective Interactions and Operators in Nuclei*, Lecture Notes in Physics 40 (Springer, Berlin, 1975), p. 250.
[26] A. V. Afanasjev, D. B. Fossan, G. J. Lane, and I. Ragnarsson, Phys. Rep. **322**, 1 (1999).
[27] W. Satula and R. Wyss, Rep. Prog. Phys. **68**, 131 (2005).
[28] J. F. Berger, M. Girod, and D. Gogny, Comput. Phys. Commun. **63**, 365 (1991).
[29] N. Schunck, J. Dobaczewski, J. McDonnell, J. Móre, W. Nazarewicz, J. Sarich, and M. V. Stoitsov, Phys. Rev. C **81**, 024316 (2010).
[30] J. Dobaczewski, J. Dudek, and R. Wyss, Phys. Rev. C **67**, 034308 (2003).
[31] A. V. Afanasjev, P. Ring, and I. Ragnarsson, *Proc. Int. Workshop PINGST2000 "Selected topics on $N = Z$ nuclei," 2000, Lund, Sweden*, edited by D. Rudolph and M. Hellström (2000), p. 183.
[32] M. A. Deleplanque, S. Frauendorf, V. V. Pashkevich, S. Y. Chu, and A. Unzhakova, Phys. Rev. C **69**, 044309 (2004).
[33] G. A. Lalazissis, S. Karatzikos, R. Fossion, D. Pena Arteaga, A. V. Afanasjev, and P. Ring, Phys. Lett. B **671**, 36 (2009).
[34] A. V. Afanasjev, J. König, P. Ring, L. M. Robledo, and J. L. Egido, Phys. Rev. C **62**, 054306 (2000).
[35] I. Ragnarsson, Nucl. Phys. A **557**, c167 (1993).
[36] A. Bohr and B. Mottelson, *Nuclear Structure* (Benjamin, New York, 1975), Vol. II.
[37] K.-K. Kan and J. J. Griffin, Phys. Rev. C **15**, 1126 (1977).
[38] M. Durand, P. Schuck, and J. Kunz, Nucl. Phys. A **439**, 263 (1985).
[39] I. N. Mikhailov, P. Quentin, and D. Samsoen, Nucl. Phys. A **627**, 259 (1997).
[40] H. Laftchiev, D. Samsoen, P. Quentin, and I. N. Mikhailov, Phys. Rev. C **67**, 014307 (2003).
[41] M. Radomski, Phys. Rev. C **14**, 1704 (1976).
[42] P. Gulshani and D. J. Rowe, Can. J. Phys. **56**, 468 (1978).
[43] P. Gulshani and D. J. Rowe, Can. J. Phys. **56**, 480 (1978).
[44] J. Kunz and U. Mosel, Nucl. Phys. A **323**, 271 (1979).
[45] J. Fleckner, J. Kunz, U. Mosel, and E. Wuest, Nucl. Phys. A **339**, 227 (1980).
[46] C. E. Svensson *et al.*, Phys. Rev. Lett. **82**, 3400 (1999).
[47] G. A. Lalazissis, J. König, and P. Ring, Phys. Rev. C **55**, 540 (1997).
[48] M. M. Sharma, M. A. Nagarajan, and P. Ring, Phys. Lett. B **312**, 377 (1993).
[49] M. Rufa, P.-G. Reinhard, J. A. Maruhn, W. Greiner, and M. R. Strayer, Phys. Rev. C **38**, 390 (1988).
[50] Q. A. Ijaz *et al.*, Phys. Rev. C **80**, 034322 (2009).
[51] T. Troudet and R. Arvieu, Ann. Phys. **134**, 1 (1981).
[52] S. G. Nilsson and I. Ragnarsson, *Shapes and Shells in Nuclear Structure* (Cambridge University Press, New York, 1995).
[53] J. J. Valiente-Dobón *et al.*, Phys. Rev. Lett. **95**, 232501 (2005).
[54] Z. Szymanski, in *Oxford Studies in Physics* (Claredon Press, Oxford, 1983).

[55] C. G. Andersson, G. Hellström, G. Leander, I. Ragnarsson, S. Åberg, J. Krumlinde, S. G. Nilsson, and Z. Szymański, Nucl. Phys. A **309**, 141 (1978).
[56] P. Ring and P. Schuck, *The Nuclear Many-Body Problem* (Springer-Verlag, Heidelberg, 1980).
[57] M. J. A. de Voigt, J. Dudek, and Z. Szymański, Rev. Mod. Phys. **55**, 949 (1983).
[58] H. Zdunczuk, W. Satula, and R. A. Wyss, Phys. Rev. C **71**, 024305 (2005).
[59] P. Ring, Y. K. Gambhir, and G. A. Lalazissis, Comput. Phys. Commun. **105**, 77 (1997).
[60] H. Molique, J. Dobaczewski, and J. Dudek, Phys. Rev. C **61**, 044304 (2000).
[61] W. Satula, J. Dobaczewski, W. Nazarewicz, and M. Rafalski, Phys. Rev. C **81**, 054310 (2010).
[62] C. J. Gallagher Jr. and S. A. Moszkowski, Phys. Rev. **111**, 1282 (1958).
[63] A. Goel and A. K. Jain, Phys. Rev. C **45**, 221 (1992).
[64] J. P. Boisson, R. Piepenbring, and W. Ogle, Phys. Rep. **26**, 99 (1976).
[65] D. Nosek, J. Kvasil, R. K. Sheline, P. C. Sood, and J. Nosková, Int. J. Mod. Phys. E **3**, 967 , 1994.
[66] N. D. Newby Jr., Phys. Rev. **125**, 2036 (1962).
[67] A. K. Jain, R. K. Sheline, D. M. Headly, P. C. Sood, D. G. Burke, I. Hrîvnácová, J. Kvasil, D. Nosek, and R. W. Hoff, Rev. Mod. Phys. **70**, 843 (1998).
[68] A. K. Jain, J. Kvasil, R. K. Sheline, and R. W. Hoff, Phys. Rev. C **40**, 432 (1989).
[69] L. Bennour, J. Libert, M. Meyer, and P. Quentin, Nucl. Phys. A **465**, 35 (1987).
[70] S. Frauendorf, Rev. Mod. Phys. **73**, 463 (2001).
[71] B. Singh, R. Zywina, and R. B. Firestone, Nucl. Data Sheets **97**, 241 (2002).